Micro-scale energy dissipation mechanisms during fracture in natural polyphase ceramic blocks

James D. Hogan[a,b], John G. Spray[b], Robert J. Rogers[a], Suporn Boonsue[b], Gregory Vincent[c], Markus Schneider[c]

[a] *Department of Mechanical Engineering, University of New Brunswick, Fredericton, New Brunswick E3B 5A3, Canada*
[b] *Planetary and Space Science Centre, University of New Brunswick, Fredericton, New Brunswick E3B 5A3, Canada*
[c] *French-German Research Institute of Saint-Louis, 5 rue du Général Cassagnou, 68300 Saint-Louis, France*

Abstract

The dynamic fracture of natural polyphase ceramic (granite) blocks by high-speed impact at 207 m/s, 420 m/s and 537 m/s has been investigated. An electromagnetic railgun was used as the launch system. Results reveal that the number of fragments increases substantially, and the dominant length scale in their probability distributions decreases, as the impact energy is increased. Micro-scale studies of the fracture surfaces reveals evidence of localized temperatures in excess of 2000 K brought on by frictional melting via fracturing and slip along grain boundaries in orthoclase and plagioclase and via transgranular fracture (micro-cracking) in quartz. The formation of SiO_2- and TiO_2-rich spheroids on fracture surfaces indicates that temperatures in excess of 3500 K are reached during fracture.

Keywords: sub- and supersonic impact, dynamic brittle fragmentation, railgun impact experiment, brittle fracture, thermal effects in cracking, microscale energy dissipation, planar fractures quartz, elastic heat dissipation in fracture, non-crystalline fracture.

Email address: v3679@unb.ca (James D. Hogan)

1. Introduction

The dynamic fracture and fragmentation of solids has been an area of continued research since the early works by Mott [1, 2]. The dynamic fracture of ductile materials [3–8] is better characterized and understood than in brittle materials [1–3, 9–13]. This stems from the large variability in quantifiable measurements when experiments are observed and, more importantly, repeated over a broad range of conditions for ceramics.

Many investigations into the dynamic fracture of brittle materials have been made through machining [14, 15] and, as in the present study, via high-speed impact testing. Impact testing of the fracture behaviour of natural ceramics[1] has been used to study terrestrial impacts [16], and in mining and rock blasting applications [17]. The fracture response of synthetic brittle materials[2] has been studied in crack-propagation experiments [18–21], where transparent polymethyl-methacrylate (PMMA) was used to visualize a propagating crack, and has been studied in the context of the ballistic protection of metal-ceramic or composite-ceramic shielding systems [22–29]. Most dynamic loading tests are primarily concerned with the ability of the ceramic to withstand the loading energy (e.g., defeating an incoming projectile, or fracturing under a given load of explosives). Less attention is given to characterizing the actual damage to the specimen, and often no attention is given to the complex energy dissipation processes that lead to the final damaged state. Understanding these processes will ultimately lead to more efficient use of ceramic materials and an increased performance in their application. The focus of the current investigation is on the fracture response and energy dissipation mechanisms of granite.

Energy dissipation during high-speed fracture has many forms. During impact testing some

[1] Examples include rocks, planetary regoliths, minerals.
[2] Examples include polymethyl-methacrylate (PMMA) and Al_2O_3.

of the energy of the projectile is transferred into kinetic energy of the target's ejected fragments. Nakamura and Fujiware [30] estimate roughly 1% of the initial kinetic energy is transferred into the kinetic energy of ejected fragments. Acoustic emission is also considered a comparably minor energy sink as well [31, 32]. The primary mechanism for energy dissipation in ceramics is the generation of new surface area [33] via fracture and fragmentation [3–5, 9–13, 34–36]. This, in turn, is related to crack propagation [18], flaw distribution [37], grain size [38] and crystallographic orientation [39]. Investigations of crack propagation have been made both analytically [40] and experimentally [18–21]. In impact studies (for example soda-lime glass spheres impacting glass targets [41]), three-dimension crack propagation has been studied in the form of Hertzian cracking [41–44], where the fracture surface through the body forms a geometrically self-similar cone over a wide range of impact conditions.

A bi-product of crack propagation is heat, which Griffith [40] noted could represent a significant portion of the energy dissipated during rupture (or crack extension). The study of heat dissipation at the tip of a moving crack has received attention in non-crystalline materials, such as polymethyl-methacrylate (PMMA) [45–47], glass [14, 48] and in various crystalline materials [14, 48, 49]. Weichert and Schönert [48] developed and used a radiation thermometer to record radiated heat from a crack tip for quartz and glass, and by crude comparisons with black body radiation, estimated temperatures of 3200 K for glass and 4700 K for quartz during crack tip extension. Chapman and Walton [14] performed machining experiments on quartz and various types of glasses. By measuring the emitted triboluminescence, they estimated that temperatures between 1850 K and 2300 K were realized for glass and 2800 K for quartz during the dynamic fracture (cutting) process. The goal of the current investigation is to gain further insight into the dynamic fracture of ceramics, and, in particular, micro-scale energy dissipation via heat generation, micro-cracking and micro-plastic deformation in a polyphase natural ceramic.

2. Experimental Set-Up and Analysis Methods

Experiments were conducted at the French-German Research Institute of Saint-Louis (ISL), France, using the facility's SR/3-60 electromagnetic railgun (Fig. 1) [50]. Its copper-alloy rails are encased in a non-conductive composite housing. The SR/3-60 is a segmented railgun, whereby current is delivered to the rails at multiple locations along its 2.25 m length. Multiple injections reduce resistive losses and, therefore, offer the potential of increasing launch efficiency in comparison to continuous injection at the breech [50]. The "3-60" refers to the number of separate rail-pair configurations through which the armature (projectile) makes contact; with each rail pair being oriented at 60°.

A hexagon-shaped projectile is deployed in the SR/3-60 (Fig. 2). The distance between diagonal vertices is 20 mm and the projectile length is 30 mm. Projectiles comprise a woven glass-fiber reinforced plastic composite sabot enclosing a single Cu-Cd brush, which consists of multiple fibres 32 mm in length. The total mass of the brush is ~23 g and the total mass of the projectile, including the brush, is ~45 g. The projectiles are custom-fabricated in-house. Three shots were made at muzzle velocities of 207 m/s, 420 m/s and 537 m/s (measured using Doppler radar), corresponding to kinetic energies at impact of 0.96 kJ, 3.96 kJ and 6.44 kJ. A summary of projectile values for each shot is presented in Table 1.

The polyphase ceramic (granite) targets have a density of 2600 kg/m^3. The granite mainly comprises the minerals orthoclase ($KAlSi_3O_8$, pale pink in colour), plagioclase ($NaAlSi_3O_8$ to $CaAl_2Si_2O_8$, white in colour) and quartz (SiO_2, translucent and glassy), with traces of biottite (dark brown in colour) and ilmenite ($FeTiO_3$ and black in colour). The volume percentage composition is approximately 5% mica, 50% plagioclase, 30% quartz and 15% orthoclase. Approximately 2 cm of the outer area of each target was confined between two pieces of plywood, which were mounted to the target holder (Fig. 3). This allowed the blocks to expand laterally following impact. A summary of the target dimensions and masses for each shot is given in Table 2, where *a* and *b* are the target height and width, and *z* is the target thickness.

Following each shot, fragments larger than 3 mm in length were weighed and counted using a Scientech S120 scale with resolution of $\pm 1\times10^{-4}$ g. Fragments smaller than 3 mm were sized and counted with a Parsum IPP70 gravity-feed probe.

Secondary electron (SE) and back-scattered electron (BSE) images of the ceramic fragments were obtained using a Hitachi SU-70 analytical Field Emission Scanning Electron Microscope (FESEM). The acceleration voltage range was 100 V to 30 kV with a beam current of a few nano-amperes. The resolution of the FESEM is 1.0 nm at 15 kV and 1.4 nm at a landing voltage of 1 kV. The samples were sputter coated with carbon prior to analysis to ensure conductivity.

The composition of the mineral phases was determined by Energy Dispersive X-ray Spectroscopy (EDS) using an INCAx-act LN2-free Analytical Silicon Drift Detector at 15 kV accelerating voltage and 5 nA beam current, with acquisition times of 100 s for all elements. With these conditions, weight percent chemical compound detection limits were 0.040 SiO_2, 0.063 TiO_2, 0.045 Al_2O_3, 0.110 FeO, 0.070 Cr_2O_3, 0.074 MgO, 0.080 MnO, 0.039 CaO, 0.028 Na_2O and 0.031 K_2O.

3. Experimental Results

3.1. General analysis of target damage

The damage states of the targets following each shot are shown in Fig. 4. The target impacted at 0.97 kJ (207 m/s) cracked into four, roughly equal size pieces. As the the impact energy increases (b and then in c), a fracture cone forms in each block, which then increases in volume as the impact energy is increased. The formation of a cone, or fragmentation zone as it will be referred to here is the result of Hertzian cracking [42–44]. A similar response in the present experiments is to be expected when projectiles with a hexagonal cross-section are used. The total volumes encompassed by the fragmentation zones are estimated as 1.59×10^5 mm^3 and 2.29×10^5 mm^3, corresponding to a 44 % increase, for impact energies from 3.96 kJ to 6.44 kJ, respectively.

Features of the fracture patterns in the damaged targets were examined (Fig. 4). Crater diameters of 41.3 mm and 54.6 mm, corresponding to 2.1 and 2.7 projectile diameters, were estimated on the front surface of the target for impact energies of 3.96 kJ and 6.44 kJ, respectively. The rear diameters of the fragmentation zone were estimated as 78.1 mm and 89.6 mm, corresponding to 3.9 and 4.5 projectile diameters, for impact energies of 3.96 kJ and 6.44 kJ, respectively. The Hertzian fracture angle, defined as the angle between the normal surface and the cone edge, is typically reported as 22° ±1° [44]. These angles were measured from the two targets, and an average taken from three of the largest fragments for each of the 3.96 kJ and 6.44 kJ samples. An angle of approximately 30°±2° was determined for both cases. The difference in angles might suggest that impact geometry and the use of a non-crystalline materials plays a role in the generation and propagation of Hertzian cracks. This is an area that warrants future work.

3.2. Fragmentation results

Typical fragments from these experiments are shown in Fig. 5. There was no shape variation found between each impact energy (Fig. 5a and b). The fragments have an aspect ratio close to one and primarily contain quartz (clear) and orthoclase (pale pink) on their fracture surface. Mott [1, 2] is credited with pioneering research into the dynamic fragmentation of solids. To display his fragmentation results, Mott plotted the logarithm of the cumulative number of fragments larger than the individual fragment size (r) on the independent-axis. Fragmentation data is plotted in a Mott representation in Fig. 6 for loading energies of 3.96 kJ and 6.44 kJ.

The number of fragments for 6.44 kJ loading energy is 26,733, which is 12.2 times larger than a total of 2,187 fragments for the 3.96 kJ case. This increase is much greater than the 1.44-fold increase in cone volume generated from the impacts. The largest fragment sizes are in the order of the target block thickness (55 mm).

The size distributions of the fragments are plotted in Fig. 7 for impact loadings of 3.96 kJ and 6.44 kJ. For the 0.97 kJ case, the ceramic block merely fractured into four large pieces (Fig. 4a). The ordinate axis label "$Q0$" refers to the fragment size density distribution; later "$Q3$" will be used to describe the volume density distribution. For clarity, the fragments are grouped into 42 bins. The first bin consists of fragments between $10^{0.90}$ μm and $10^{1.00}$ μm. The total number of fragments between these values are plotted at the center point of $10^{0.95}$ μm. The second bin consists of values between $10^{1.00}$ μm and $10^{1.10}$ μm, with values plotted at $10^{1.05}$ μm. The remaining data is plotted in this way. The highest percentage in the fragment-size density distribution for a loading of 6.44 kJ occurs at a smaller fragment size than for a loading of 3.96 kJ (100 μm and 178 μm, respectively). There are also smaller peaks in the distribution at 12,200 μm for 3.96 kJ and 4,470 μm for 6.44 kJ. These are believed to be associated with the numerous fragments that come from the rear surface of the target following impact. An example of one of these fragments is shown in Fig. 8.

The average fragment sizes for loading energies of 3.96 kJ and 6.44 kJ are 967 μm and 358 μm, respectively. These values are much larger than the values of the peaks in the $Q0$ distribution. This suggests that using an average value is not appropriate when determining the dominant fragment length of the whole sample. If only fragments smaller than 3 mm are considered (i.e., those that are believed to be from the fragmentation zone and, perhaps, a true measure of the dominant fragment scale) then the average fragment sizes are 382 μm for 3.96 kJ, and 209 μm for 6.44 kJ. This, once again, overestimates the dominant length scale in the sample. Together, these values indicate that larger impact energy results in a smaller dominant fragment size.

Knowing the probability distribution of the fragmentation data yields insight into the length scale distribution based on the total number of fragments generated in the dynamic event. However, for modeling purposes the number of fragments is difficult to determine and would vary greatly depending on, for example, the size of the target and the impact conditions. It is thus important to know the volume density distribution, $Q3$, for such events. Fig. 9 shows the volume density distribution of the fragments sized and counted by the gravity-feed probe (i.e., those estimated to be <3 mm, with some fragments as large as 5 mm) for the 3.96 kJ and 6.44 kJ cases. Here, only those fragments believed to be associated with the fragmentation zone are used because they are assumed to be independent of the target size, and hence useful for modeling. It was also assumed that each fragment was spherical based on their aspect rations being approximately unity. The data is separated into 32 bins and normalized over the total volume of the sample, with the first bin centered at $10^{2.05}$ μm and consisting of values between $10^{2.00}$ μm and $10^{2.10}$ μm. The other bins are organized in the same way. The peak in the $Q3$ distribution ($\approx$25% for 3.96 kJ) corresponds to a fragment size of 2,800 μm . This is larger in both value and percentage of the total volume than the peak for 6.44 kJ loading case (corresponding to 1,775 μm at $Q3$ $\approx$17%). A summary of the length scales from these experiments is shown in Table 3.

Next, the total generated fracture surface area for each case is estimated. For a loading energy of 0.97 kJ, only four fragments were generated following impact. It was assumed that each fragment was in the shape of cube, resulting in a generated surface area of 0.025 m^2. The larger fragments for the 3.96 kJ and 6.44 kJ loading cases, the ones shown in Fig. 4, were measured directly, while the fragments in the fragmentation zone were assumed to be spherical based on Fig. 5. The total surface area generated for the 3.96 kJ and 6.44 kJ cases was estimated as 0.051 m^2 and 0.126 m^2, respectively. If a fracture surface energy[3], Γ'', of 29 J/m^2 is taken then the total energy consumed by generating the fracture surfaces is 0.73 J, 1.48 J, and 3.65 J. These values represent much less than 1% of the values for the total impact energies of 0.97 kJ, 3.96 kJ and 6.44 kJ. Similar conversion values have been previously reported by Woodward et al. [53]. Realistically, this conversion is largely underestimated because, as will be shown later, high magnification of the fracture surface indicates that much more surface area is actually created. The exact amount of surface area generated during fracture for various size ranges warrants future work.

3.3. Microscale fracture surfaces and energy dissipation mechanisms

The textures and compositions on the fracture surfaces were examined using analytical scanning electron microscopy. Examples of dynamic fracture features in orthoclase, plagioclase, and quartz for an impact energy of 6.44 kJ are shown in Fig. 10a, c and e, respectively. Fracture in the orthoclase is primarily via mode 1 transgranular fracture that occurs along cleavage planes, which are parallel to crystallographic faces {001} and {010} (Fig. 10a). The step-height is roughly 120 μm at this scale. Fracture in the plagioclase (Fig. 10c) occurs along cleavage planes, with some fracture across the cleavage planes (mainly {001}), as indicated by uneven fractured surfaces. The thickness of each of the cleavage planes in roughly 3.5 μm. Dynamic fracture associated with quartz occurs primarily along grain boundaries (intergranular), with fracturing also occurring along inherent flaws in the grain (transgranular) (Fig. 10e).

Fracture surfaces in orthoclase, plagioclase and quartz are further revealed in Fig. 10b, d and f. Cleavage fracture patterns in orthoclase are shown at this scale, with local areas of roughened patterns indicated by arrows (Fig. 10b). In the plagioclase, there is evidence of

---

[3] $\Gamma''=K_c^2/2B_o$ [12], where K_c=1.79 MPa $\sqrt{m}$ [51] is the fracture toughness, ρ=2,600 kg/m^3 is the density, and $c=\sqrt{B_o/\rho}$=4,620 m/s, where B_o is the bulk modulus and is taken as 55.5 GPa [52].

localized melt/plastic deformation at grain or crystal boundaries (Fig. 10d). Cracks are seen in the quartz samples with elevated roughened edges crossing at 90° to each other (Fig. 10f).

3.3.1. Localized heat dissipation on fracture surfaces

Evidence of localized melting in a quartz grain micro-crack is shown Fig. 11a in the form of an SiO_2-connection and glass deposit between the adjacent cracked edges. The distance between these surfaces is about 1 μm. Temperatures needed to melt quartz are approximately 2000 K [54]. Evidence of higher localized temperatures are indicated in Fig. 11b in the form of a TiO_2-rich spheroid (derived from $FeTiO_3$ ilmenite breakdown to FeO and TiO_2), approximately 4 μm in diameter. The temperature needed to vaporize and cause the breakdown of ilmenite is in the order of 3000 K [55]. Results here suggest that these localized temperatures are reached during the high-speed impact tests and, more specifically, during the fracture process.

More evidence of high localized temperatures at the microscale in the form of plagioclase-like and alkali-felspar-like spheroids are shown in Fig. 11c and d. The albite spheroid in Fig. 11c is approximately 1.0 μm in diameter, while the orthoclase spheroid in Fig. 11d is roughly 8.0 μm in diameter. Temperatures in excess of 3500 K [54] are needed to vaporize these silicate minerals. An additional spheroid composed of alkali-feldspar-like mineral, and a CuO spheroid are shown in Fig. 11e and f, respectively. The CuO-rich spheroid is derived from the vaporization and re-condensation of the copper brushes from the projectile. Typical orthoclase and plagioclase mineral compositions and corresponding compound-% of oxides in each of the spheroids and glass from Fig. 11 are given in Table 4.

4. Discussion

The dynamic fragmentation experiments indicate that an increase in impact energy results in a dramatic increase in the number of fragments and, more specifically, the generated surface area. The generation of more fragments, for a small increase in the fragmentation zone volume, resulted in a decrease in the dominant fragment size for the two cases studied.

The primary focus of this study was to examine micro-scale energy dissipation mechanisms on fracture surfaces. Roughened areas over a large landscape of local fracture surfaces in plagioclase and orthoclase (Fig. 10b and c) suggest the action of intragrain motions/vibrations operating prior to fragmentation. Evidence of localized melting and/or plastic deformation at these boundaries is presented in Fig. 10d; again suggesting that grain motion, and subsequent frictional heating, occurs during and possible just after fracture.

Micro-cracking in quartz (Fig. 10f) reveals evidence of roughened surfaces on adjacent cracked edges brought on by motion/vibration. Fig. 10a extends this discussion and suggests that friction between these two sides, or the generation of the micro-crack itself, provides a very localized energy source great enough to melt the quartz (>2000 K [54]). Further evidence of very localized temperatures in the order of 3500 K are suggested by the formation of the spheroids on the fracture surface (Fig. 11b to f). Energies required to form these spheroids represent a small portion of the incoming kinetic energy of the projectile.

5. Conclusions

The dynamic fracture of natural polyphase ceramic blocks subjected to high-speed impact was investigated experimentally for impact loadings of 0.97 kJ, 3.96 kJ, and 6.44 kJ. Fragmentation results indicate that the onset of fragmentation in the ceramic occurs at a loading energy between 0.97 kJ and 3.96 kJ. As the impact energy is increased beyond this critical value, the number of generated fragments increases and the dominant length scale in their distributions decreases.

Micro-scale energy dissipation on the fracture surfaces of the granite fragments were also examined. Evidence of melt and plastic deformation along grain boundaries and in transgranular fracture (micro-cracking in quartz and rupturing in orthoclase and plagioclase) indicate that frictional heating caused by adjacent fracture surface motions result in temperatures greater than 2000 K. The formation of SiO_2- and TiO_2-rich spheroids on fracture surfaces indicate that temperatures in excess of 3500 K were reached during fracture.

6. Acknowledgment

This work was supported by a Natural Sciences and Engineering Research Council (NSERC) CGS-M scholarship to JDH and funding from NSERC, the Canada Research Chairs program and the Canada Foundation for Innovation to JGS. Alan Rawle of Malvern Instruments, Massachusetts, is thanked for performing the Parsum IPP70 analysis. Planetary and Space Science Centre contribution 47.

7. References

[1] N. Mott, A theory of the fragmentation of shells and bombs, Technical Report AC4035, United Kingdom Ministry of Supply (May 1943).

[2] N. Mott, Fragmentation of shell cases, Technical Report A189: 300308, Proceedings of the Royal Society (1947).

[3] D. Grady, The spall strength of condensed matter, Journal of Mechanics Physics of Solids 36 (1988) 353–384.

[4] D. E. Grady, Local inertial effects in dynamic fragmentation, Journal of Applied Physics 53 (1) (1982) 322–325.

[5] M. Meyers, K. Chawla, Mechanical Behavior of Materials, 2nd Edition, Cambridge, United Kingdom, 2009.

[6] B. J. Campbell, A. Dowling, The behaviour of materials subjected to dynamic incremental shear loading, Journal of the Mechanics and Physics of Solids 18 (1) (1970) 43 – 63.

[7] J. Campbell, Dynamic plasticity: Macroscopic and microscopic aspects, Materials Science and Engineering 12 (1) (1973) 3 – 21.

[8] T. Sakai, Dynamic recrystallization: Mechanical and microstructural considerations, Acta Metallurgica 32 (2) (1984) 189 – 209.

[9] S. Levy, J. Molinari, Dynamic fragmentation of ceramics, signature of defects and scaling of fragment sizes, Journal of the Mechanics and Physics of Solids 58 (1) (2010) 12 – 26.

[10] D. Grady, M. Kipp, The micromechanics of impact fracture of rock, International Journal of Rock Mechanics 16 (5) (1979) 293 – 302.

[11] D. Shockey, D. Curran, L. Seaman, Fragmentation of rock under dynamic loads, International Journal of Rock Mechanics and Mining Sciences and Geomechanics Abstracts 11 (12) (1974) 250.

[12] D. Grady, Length scales and size distributions in dynamic fragmentation, International Journal of Fracture 163 (1–2) (2009) 85–99.

[13] D. Grady, Fragment size distributions from the dynamic fragmentation of brittle solids, International Journal of Impact Engineering 35 (12) (2008) 1557 – 1562, hypervelocity Impact Proceedings of the 2007 Symposium - HVIS 2007.

[14] G. N. Chapman, A. J. Walton, Triboluminescence of glasses and quartz, Journal of Applied Physics 54 (10) (1983) 5961 – 5965.

[15] R. Chauhan, Y. Ahn, S. Chandrasekar, T. Farris, Role of indentation fracture in free abrasive machining of ceramics, Wear 162-164 (Part 1) (1993) 246 – 257.

[16] B. J. Gladman, J. A. Burns, M. Duncan, P. Lee, H. F. Levison, The Exchange of Impact Ejecta Between Terrestrial Planets, Science 271 (5254) (1996) 1387–1392.

[17] J. Aler, J. D. Mouza, M. Arnould, Measurement of the fragmentation efficiency of rock mass blasting and its mining applications, International Journal of Rock Mechanics and Mining Science and Geomechanics Abstracts 33 (2) (1996) 125 – 139.

[18] E. Sharon, S. P. Gross, J. Fineberg, Energy dissipation in dynamic fracture, Phys. Rev. Lett. 76 (12) (1996) 2117–2120.

[19] K. Ravi-Chandar, W. G. Knauss, An experimental investigation into dynamic fracture: III. on steady-state crack propagation and crack branching, International Journal of Fracture 26 (1984) 141–154.

[20] S. P. Gross, J. Fineberg, M. Marder, W. D. McCormick, H. L. Swinney, Acoustic emissions from rapidly moving cracks, Phys. Rev. Lett. 71 (19) (1993) 3162–3165.

[21] J. Fineberg, S. P. Gross, M. Marder, H. L. Swinney, Instability in the propagation of fast cracks, Phys. Rev. B 45 (10) (1992) 5146–5154.

[22] E. S. C. Chin, Army focused research team on functionally graded armor composites, Materials Science and Engineering A 259 (2) (1999) 155 – 161.

[23] B. A. Gama, T. A. Bogetti, B. K. Fink, C.-J. Yu, T. D. Claar, H. H. Eifert, J. W. Gillespie, Aluminum foam integral armor: a new dimension in armor design, Composite Structures 52 (3-4) (2001) 381 – 395.

[24] E. Strassburger, Ballistic testing of transparent armour ceramics, Journal of the European Ceramic Society 29 (2) (2009) 267 – 273, special Issue on Transparent Ceramics.

[25] D. P. Goncalves, F. C. L. de Melo, A. N. Klein, H. A. Al-Qureshi, Analysis and investigation of ballistic impact on ceramic/metal composite armour, International Journal of Machine Tools and Manufacture 44 (2-3) (2004) 307 – 316.

[26] D. J. Viechnicki, A. A. Anctil, D. J. Papetti, Lightweight armor a progress report, Progress report US Army MTL TR 89-8;, US Army (1989).

[27] D. A. Shockey, A. Marchand, S. Skaggs, G. Cort, M. Burkett, R. Parker, Failure phenomenology of confined ceramic targets and impacting rods, International Journal of Impact Engineering 9 (3) (1990) 263 – 275.

[28] M. L. Wilkins, Mechanics of penetration and perforation, International Journal of Engineering Science 16 (11) (1978) 793 – 807, special Issue: Penetration Mechanics.

[29] M. L. Wilkins, C. F. Cline, C. A. Honodel, Fourth progress report of light armour program, Tech. Rep. Report UCRL 50694, Lawrence Radiation Laboratory, Livermore, CA (1969).

[30] A. Nakamura, A. Fujiwara, Velocity distribution of fragments formed in a simulated collisional disruption, Icarus 92 (1) (1991) 132 – 146.

[31] D. Lockner, The role of acoustic emission in the study of rock fracture, International Journal of Rock Mechanics and Mining Sciences and Geomechanics Abstracts 30 (7) (1993) 883 – 899.

[32] A. G. Evans, M. Linzer, Acoustic emission in brittle materials, Annual Review of Materials Science 7 (1) (1977) 179–208.

[33] S. M. Wiederhorn, Fracture surface energy of glass, Journal of the American Ceramic Society 52 (2) (1969) 99–105.

[34] D. E. Grady, D. A. Benson, Fragmentation of metal rings by electromagnetic loading, Experimental Mechanics 23 (4) (1983) 393–400.

[35] M. A. Meyers, C. T. Aimone, Dynamic fracture (spalling) of metals, Progress in Materials Science 28 (1) (1983) 1 – 96.

[36] G. R. Johnson, W. H. Cook, Fracture characteristics of three metals subjected to various strains, strain rates, temperatures and pressures, Engineering Fracture Mechanics 21 (1) (1985) 31 – 48.

[37] C. Johnson, Fracture statistics of multiple flaw distributions, Fracture Mechanics of Ceramics Vol. 5. Surface Flaws, Statistics and Microcracking. 76 (12) (1981) 2117–2120.

[38] R. W. Rice, C. C. Wu, F. Boichelt, Hardnessgrain-size relations in ceramics, Journal of the American Ceramic Society 77 (10) (1994) 2539–2553.

[39] R. Armstrong, E. Raymond, R. Vandervoot, Anomalous increase in hardness with increase in grain size of beryllia, Journal of the American Ceramic Society 53 (9) (1970) 529–530.

[40] A. A. Griffith, The phenomena of rupture and flow in solids, Philosophical Transactions of the Royal Society of London. Series A, Containing Papers of a Mathematical or Physical Character 221 (1921) pp. 163–198.

[41] M. Chaudhri, C. Liangyi, The orientation of the hertzian cone crack in soda-lime glass formed by oblique dynamic and quasi-static loading with a hard sphere, Journal of Materials Science 24 (1989) 3441–3448.

[42] C. G. Knight, M. V. Swain, M. M. Chaudhri, Impact of small steel spheres on glass surfaces, Journal of Materials Science 12 (1977) 1573–1586.

[43] C. Kocer, R. E. Collins, Angle of hertzian cone cracks, Journal of the American Ceramic Society.

[44] B. R. Lawn, Hertzian fracture in single crystals with the diamond structure, Journal of Applied Physics 39 (10) (1968) 4828 –4836.

[45] W. Dll, Kinetics of crack tip craze zone before and during fracture, Polymer Engineering and Science 24 (10) (1984) 798–808.

[46] D. Rittel, Experimental investigation of transient thermoplastic effects in dynamic fracture, International Journal of Solids and Structures 37 (21) (2000) 2901 – 2913.

[47] K. N. G. Fuller, P. G. Fox, J. E. Field, The temperature rise at the tip of fast-moving cracks in glassy polymers, Proceedings of the Royal Society of London. Series A, Mathematical and Physical Sciences 341 (1627) (1975) pp. 537–557.

[48] R. Weichert, K. Schnert, Heat generation at the tip of a moving crack, Journal of the Mechanics and Physics of Solids 26 (3) (1978) 151 – 161.

[49] P. G. Fox, J. Soria-Ruiz, Fracture-induced thermal decomposition in brittle crystalline solids, Proceedings of the Royal Society of London. Series A, Mathematical and Physical Sciences 317 (1528) (1970) pp. 79–90.

[50] S. Hundertmark, G. Vincent, Performance of a hexagonal, segmented railgun, IET Conference Publications 2009 (CP553) (2009) 23.

[51] P. G. Meredith, B. K. Atkinson, Fracture toughness and subcritical crack growth during high-temperature tensile deformation of westerly granite and black gabbro, Physics of the Earth and Planetary Interiors 39 (1) (1985) 33 – 51.

[52] H. Ai, T. Ahrens, Simulation of dynamic response of granite: A numerical approach of shock-induced damage beneath impact craters, International Journal of Impact Engineering 33 (1-12) (2006) 1 – 10, hypervelocity Impact Proceedings of the 2005 Symposium.

[53] R. Woodward, W. Gooch, Jr, R. O'Donnell, W. Perciballi, B. Baxter, S. Pattie, A study of fragmentation in the ballistic impact of ceramics, International Journal of Impact Engineering 15 (5) (1994) 605 – 618.

[54] T. J. Ahrens, J. D. O'Keefe, Shock melting and vaporization of lunar rocks and minerals, Earth, Moon, and Planets 4 (1972) 214–249.

[55] P. Eckhard (Ed.), Lunar Resource Utilization. In: The Lunar Handbook, Space and Technology Series, McGraw-Hill, New York, 1999, pp. 607–663.

List of Figures and Tables

Click here to download e-component: List_Tables_Figures.pdf

These are the tables

Table 1: Projectile values for each trial.

Trial number	mass of projectile mass (g)	v (m/s)	KE of projectile (kJ)	Mach number
1	45.3	207	0.97	0.6 subsonic
2	44.9	420	3.96	1.2 transonic
3	44.7	537	6.44	1.6 supersonic

Table 2: Target values for each shot.

Shot number	$a \times b$ (mm)	z (mm)	mass of target (kg)
1	115×112	55	1.845
2	109×112	55	1.750
3	113×112	55	1.807

Table 3: A summary of dominant fragment size values.

	0.97 kJ	3.96 kJ	6.44 kJ
No. of frag'ts	4	2,187	26,733
Peak $Q0$	–	178 μm	100 μm
Avg. $<$ 3 mm	–	382 μm	209 μm
Avg.	–	967 μm	358 μm
Peak $Q3$	–	2,800 μm	1,775 μm

Table 4: Compound-% of typical mineral compositions, melt and spheroids from Fig. 11.

	plagioclase mineral	alkali-feldspar mineral	(a) SiO_2 glass	(b) TiO_2 spheroid	(c) plagioclase-like spheroid	(d) akali-feldspar-like spheroid	(e) akali-feldspar-like spheroid	(f) CuO spheroid
SiO_2	68.37	67.20	100.00	3.83	72.84	58.93	52.22	3.44
TiO_2	0.00	0.00	0.00	89.45	0.00	0.00	0.00	0.00
Al_2O_3	19.28	17.91	0.00	4.00	21.69	24.74	14.48	0.64
FeO	0.00	0.00	0.00	0.83	0.00	0.00	0.29	0.00
MgO	0.00	0.00	0.00	0.25	0.00	0.00	1.06	0.00
MnO	0.00	0.00	0.00	0.04	0.00	1.35	0.00	0.00
CaO	1.60	0.00	0.00	0.69	0.49	0.00	1.35	0.00
Na_2O	9.89	3.21	0.00	0.28	4.56	5.36	3.45	0.00
K_2O	0.85	11.68	0.00	0.36	0.42	5.21	14.78	0.00
P_2O_5	0.00	0.00	0.00	0.00	0.00	0.00	12.16	0.00
BaO	0.00	0.00	0.00	0.28	0.00	4.42	0.20	0.00
CuO	0.00	0.00	0.00	0.00	0.00	0.00	0.00	95.91

Fig. 1. The SR/3-60 electromagnetic launcher.

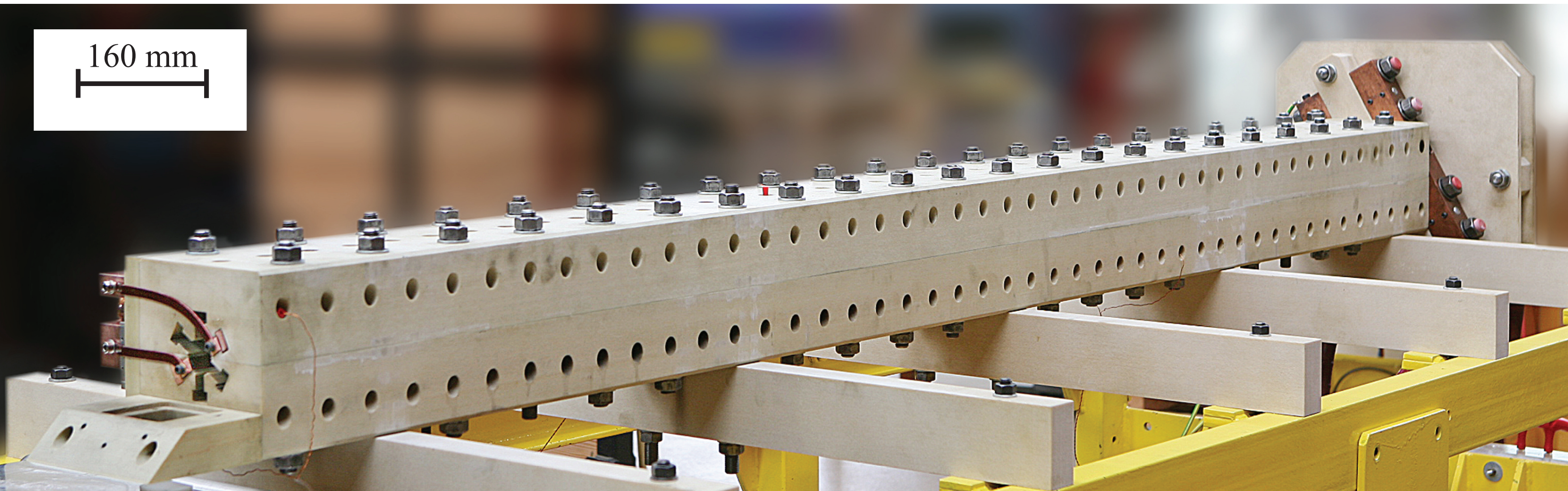

Fig. 2. Projectile type used with the SR/3-60

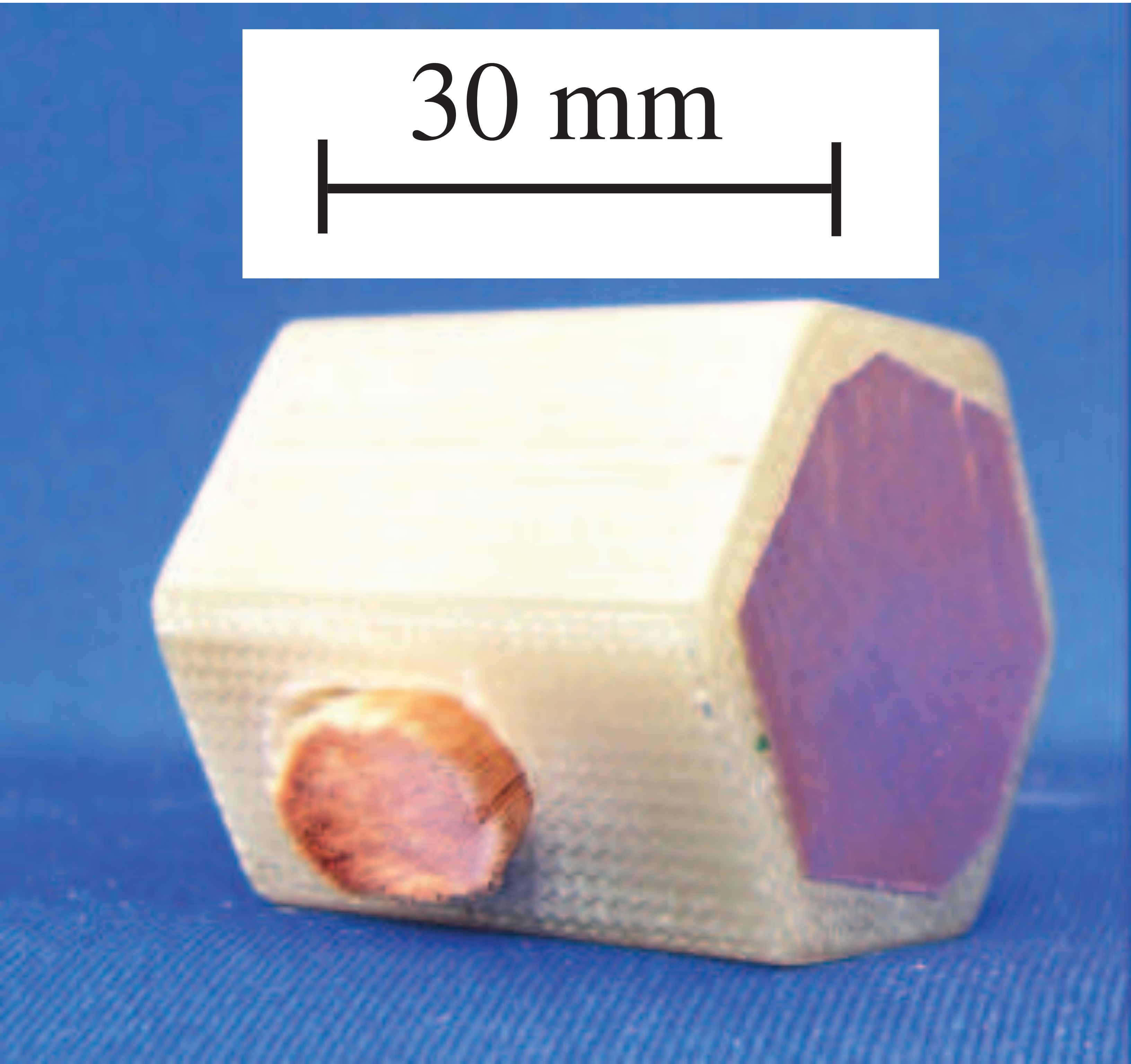

Fig. 3. Photograph of target set-up.

Fig. 4a. Front side of impacted target for 0.97 kJ loadi

Fig. 4b. Back side of impacted target for 0.97 kJ loading.

Back

112 mm

Fig. 4c. Front side of impacted target for 3.96 kJ loading.

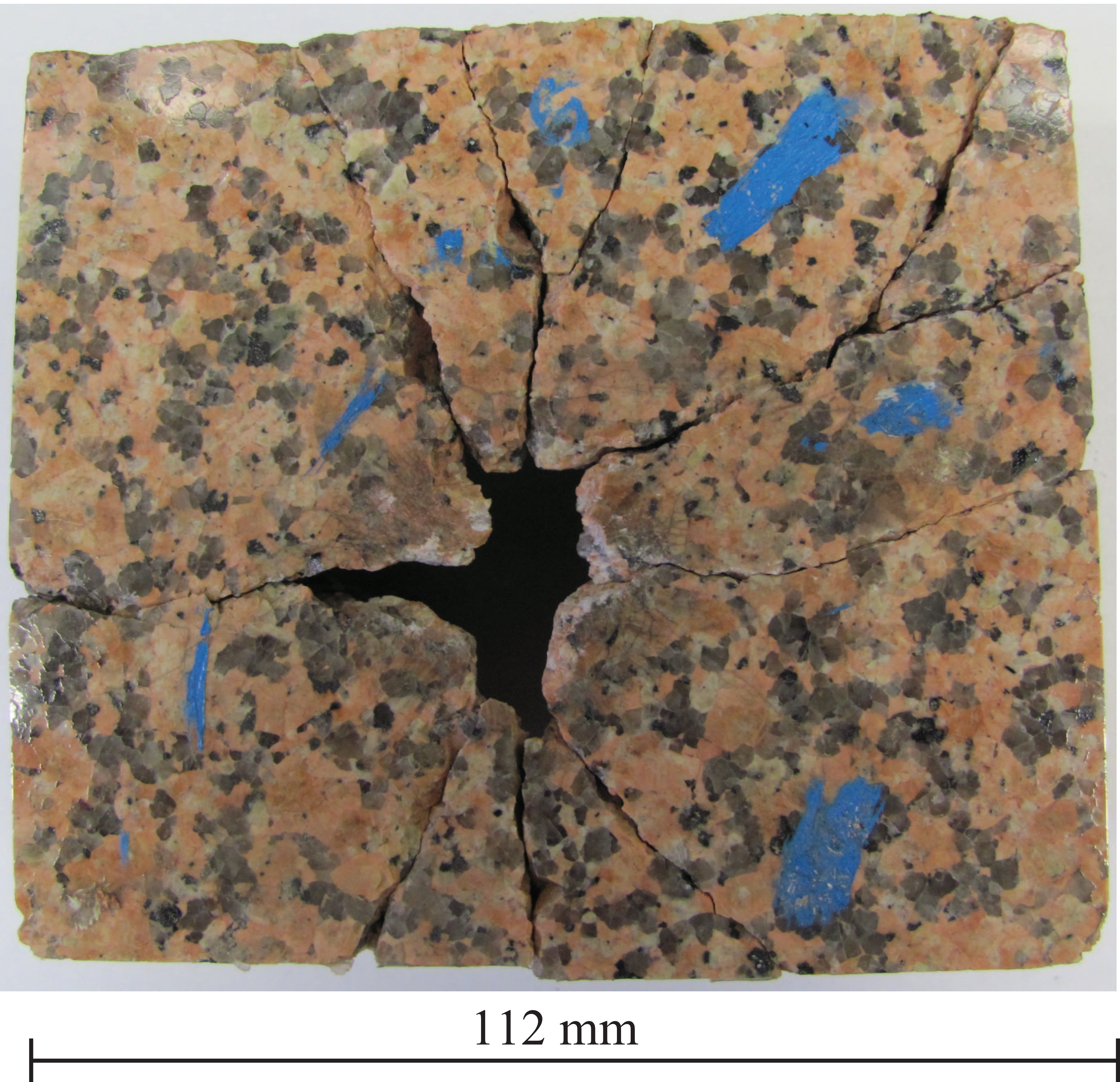

Fig. 4d. Back side of impacted target for 3.96 kJ loading.

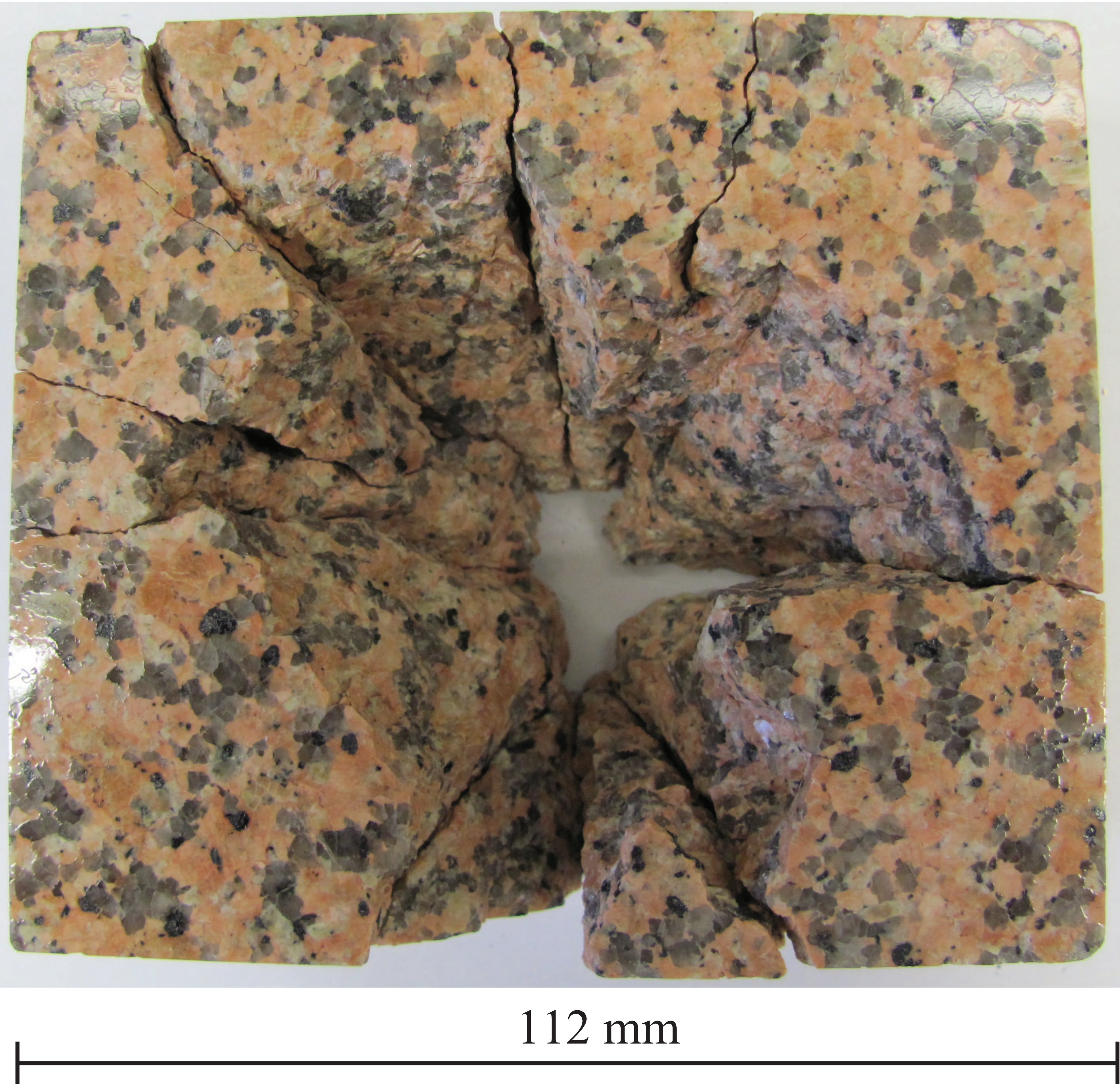

Fig. 4e. Front side of impacted target for 6.44 kJ loading.

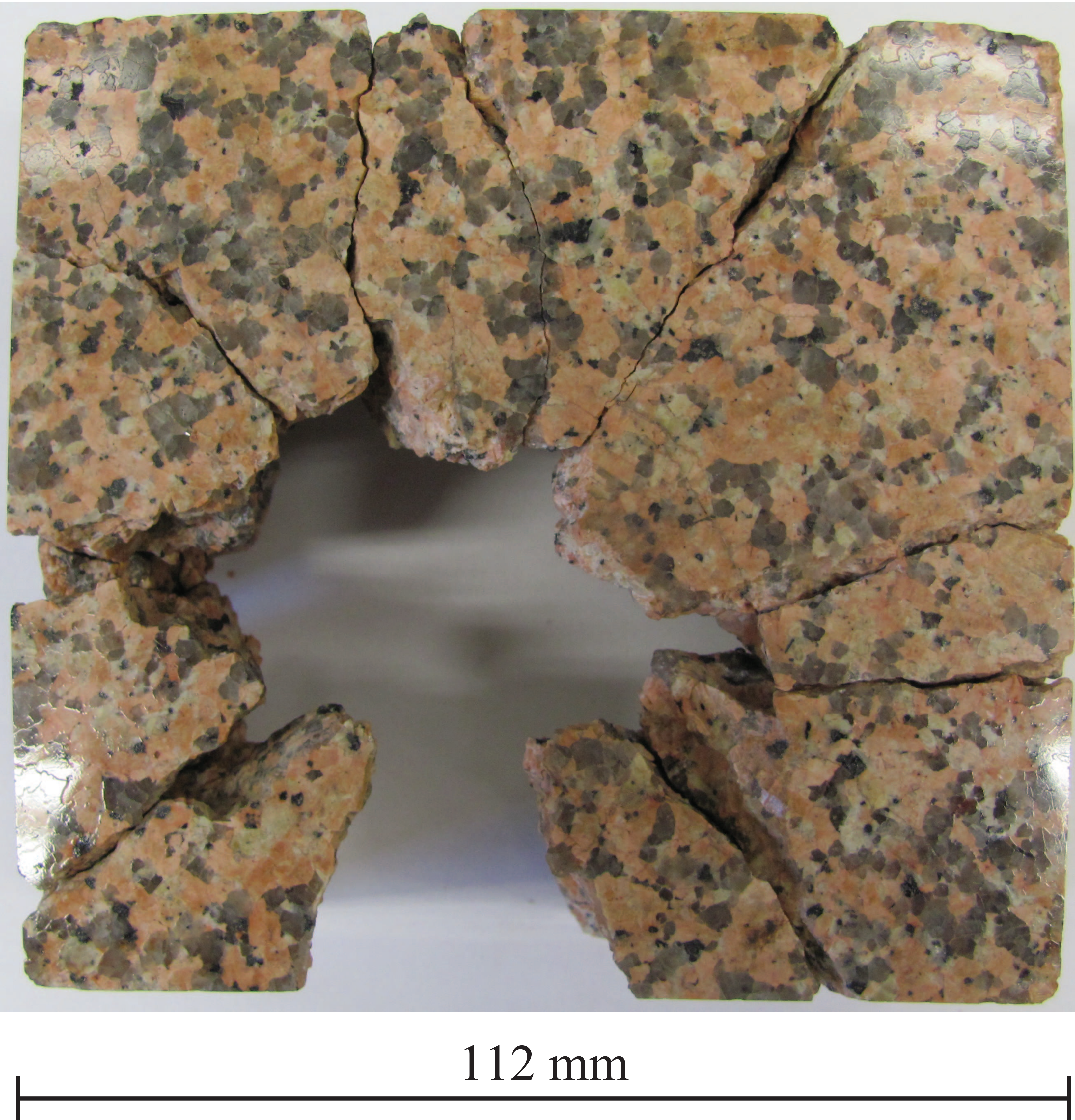

Fig. 4f. Back side of impacted target for 6.44 kJ loading.

Fig. 5a. Photograph of typical fragments for 6.44 kJ.

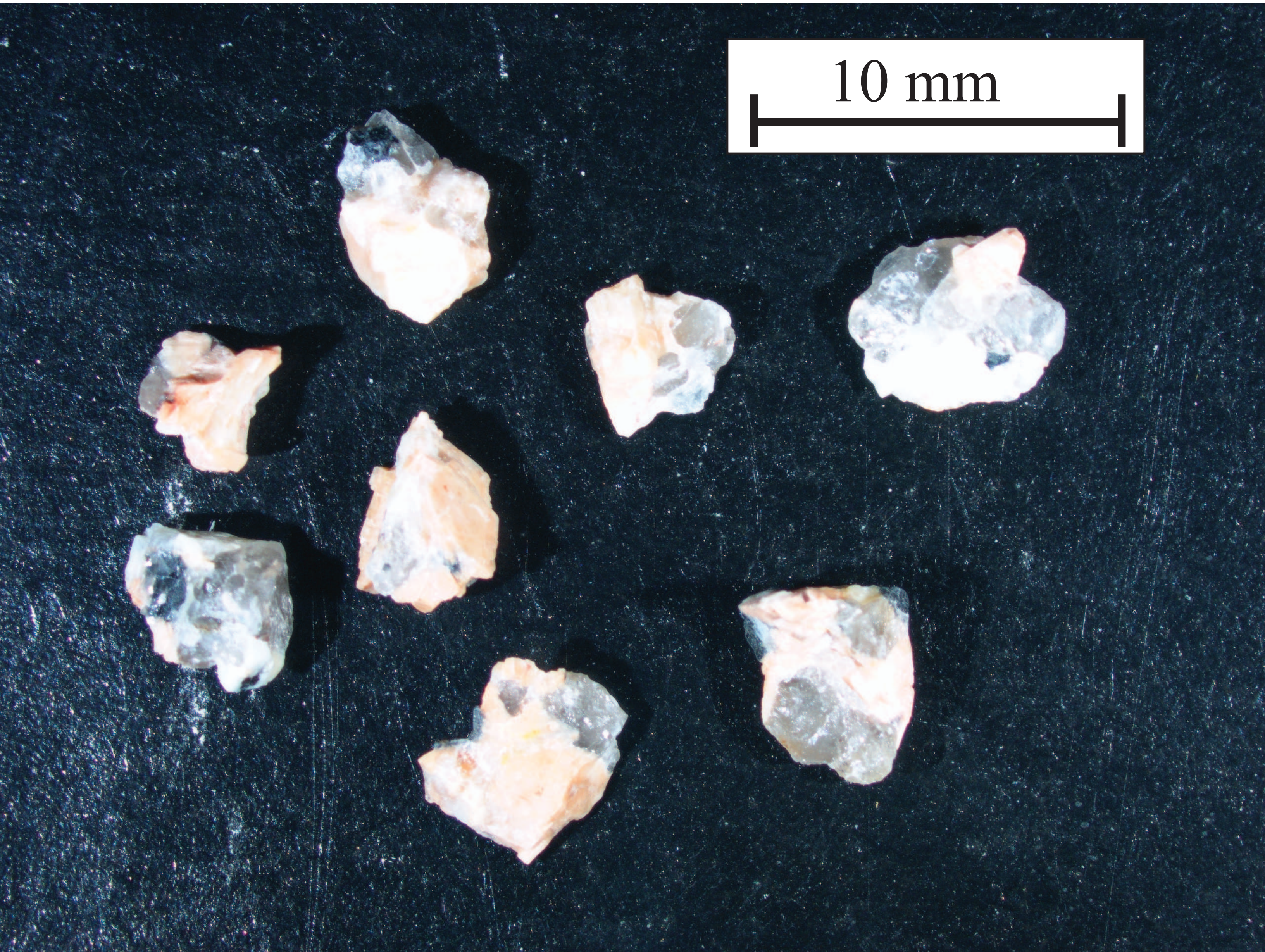

Fig. 5b. Photograph of typical fragments for 6.44 kJ.

Fig. 5c. Photograph of typical fragments for 3.96 kJ.

Fig. 5d. Photograph of typical fragments for 3.96 kJ.

Fig. 6. Mott plot of fragmentation data.

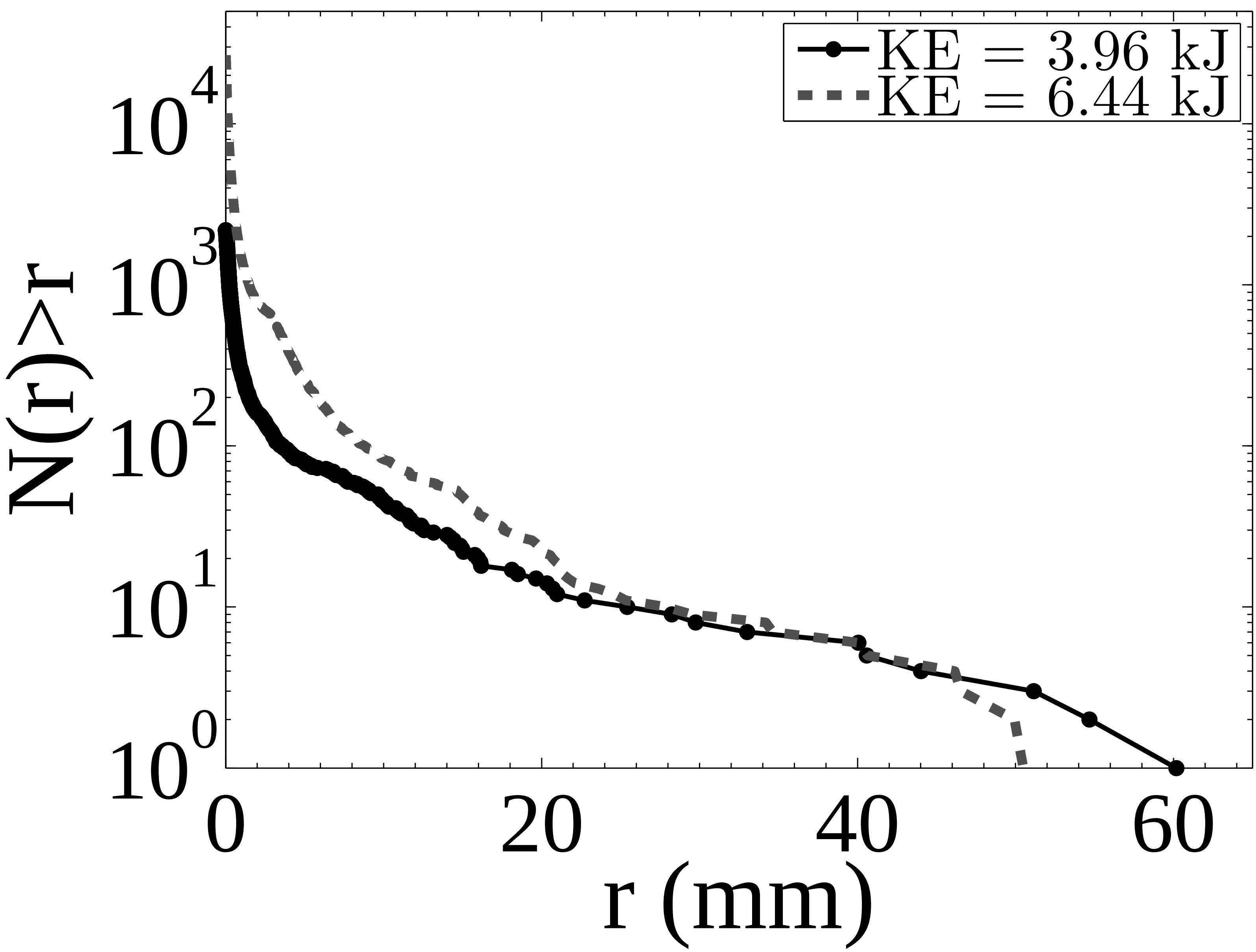

Fig. 7. Probability density distribution of fragments.

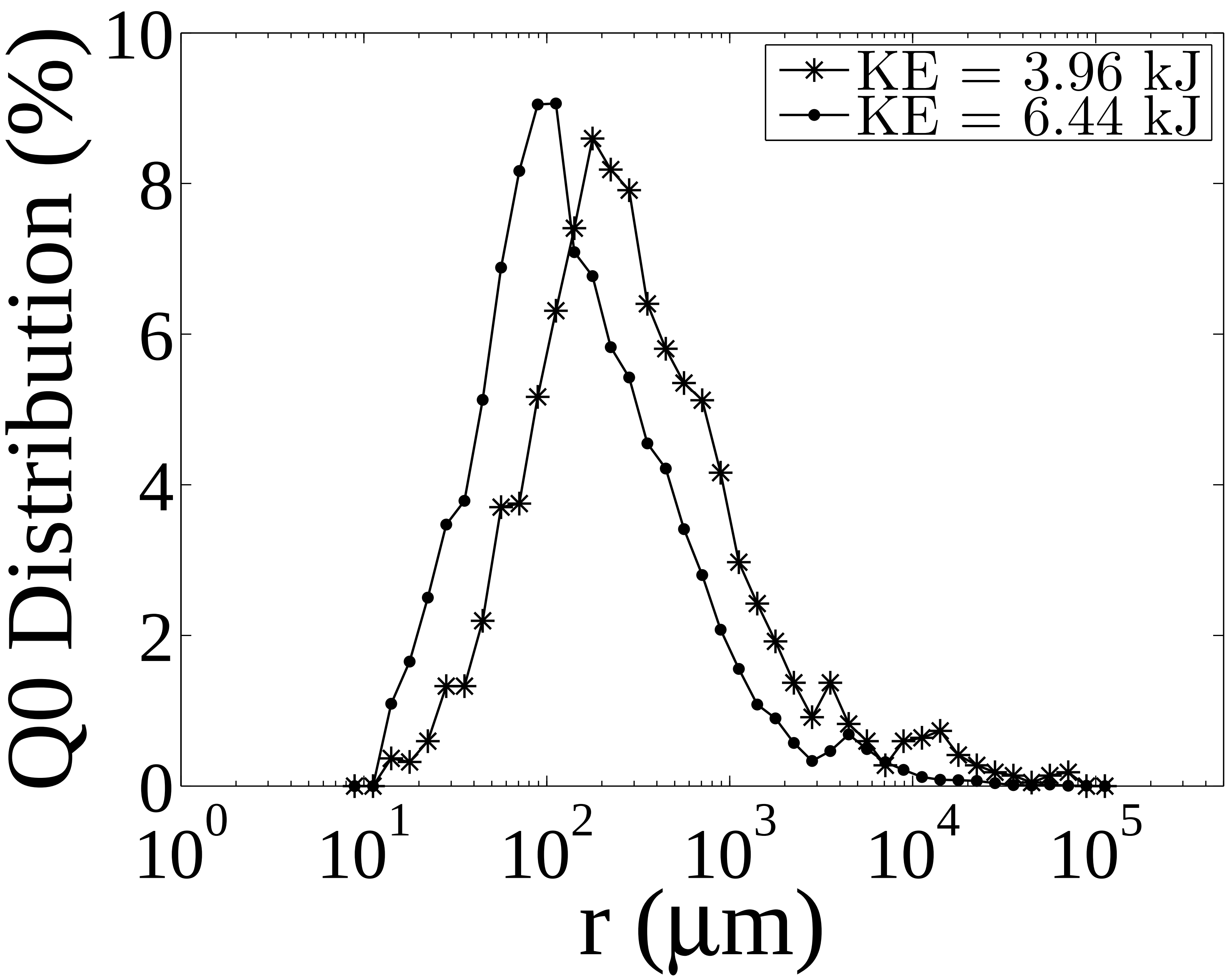

Fig. 8. Typical fragment from the back of the target.

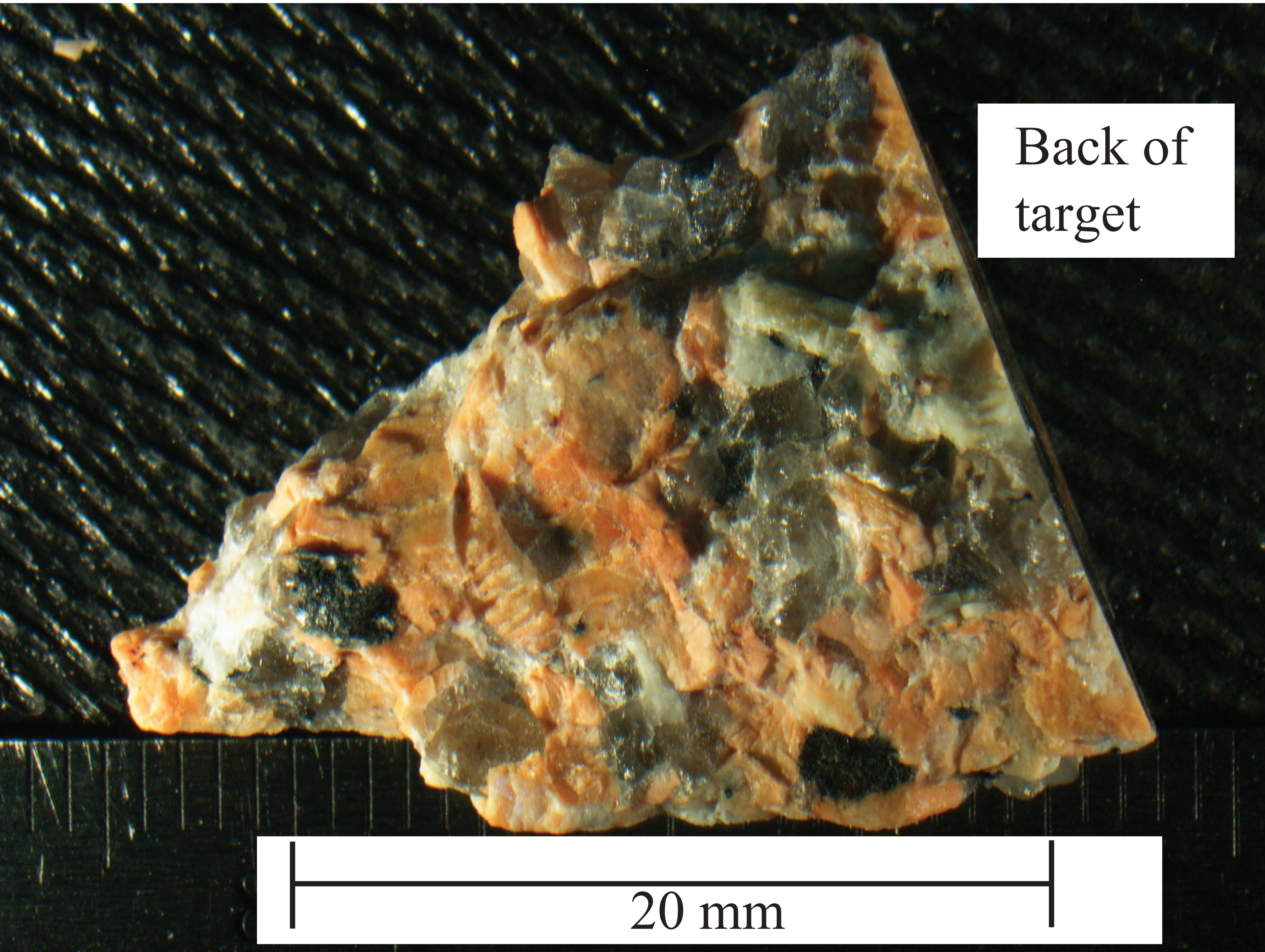

Fig. 9. Volume density distribution

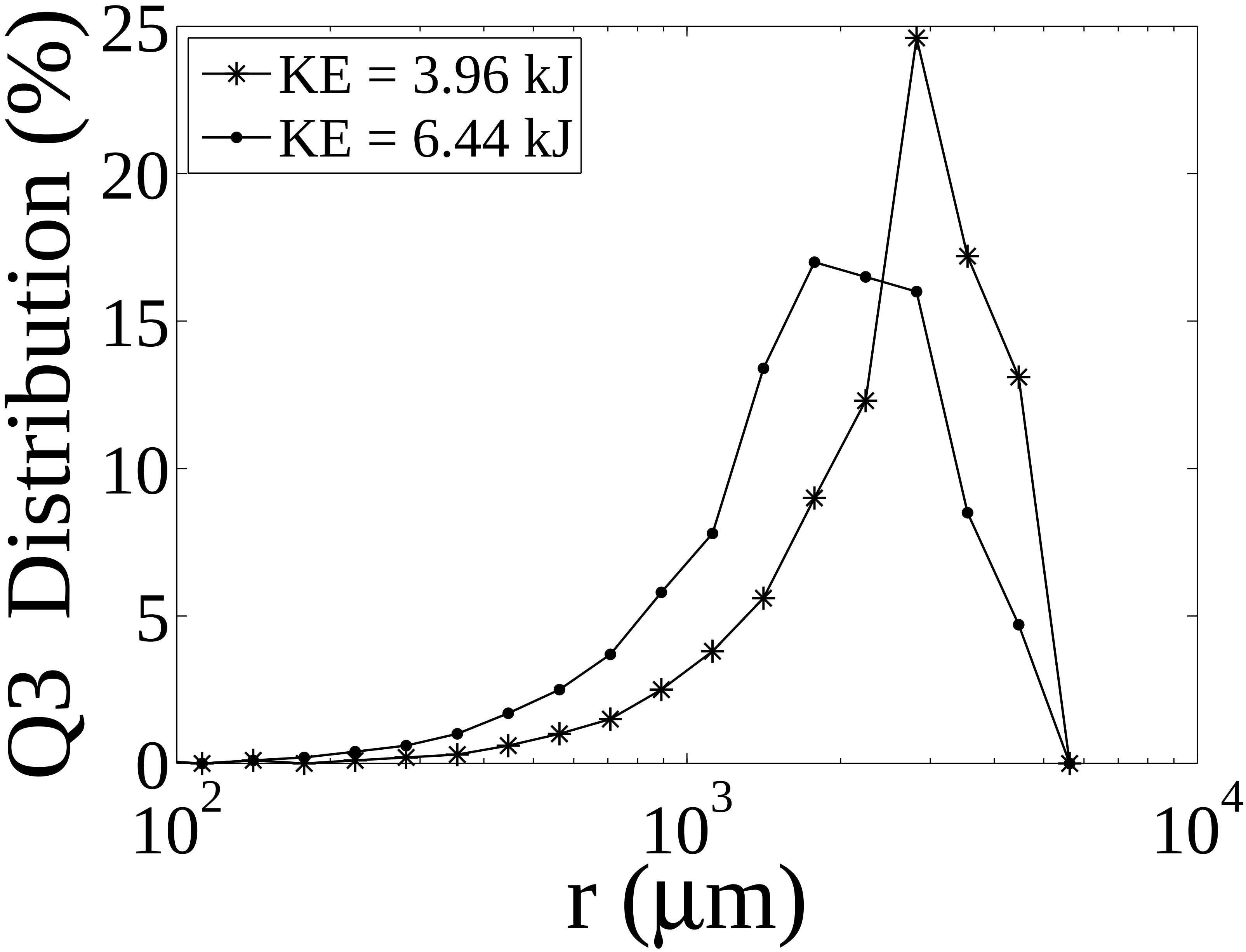

Fig. 10a. SEM image of dynamic fracture features in orthoclase.

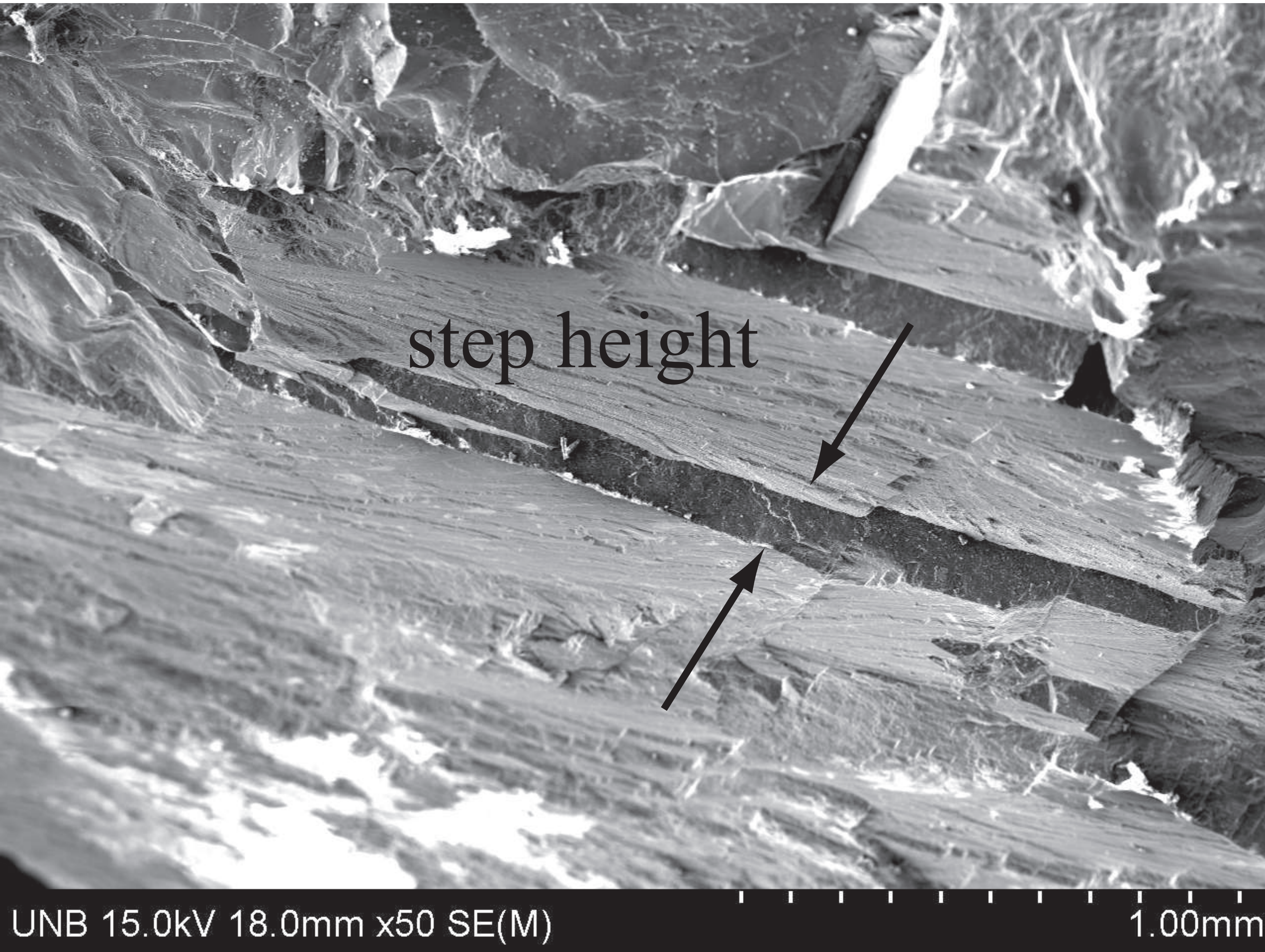

Fig. 10b. SEM image of dynamic fracture features in orthoclase.

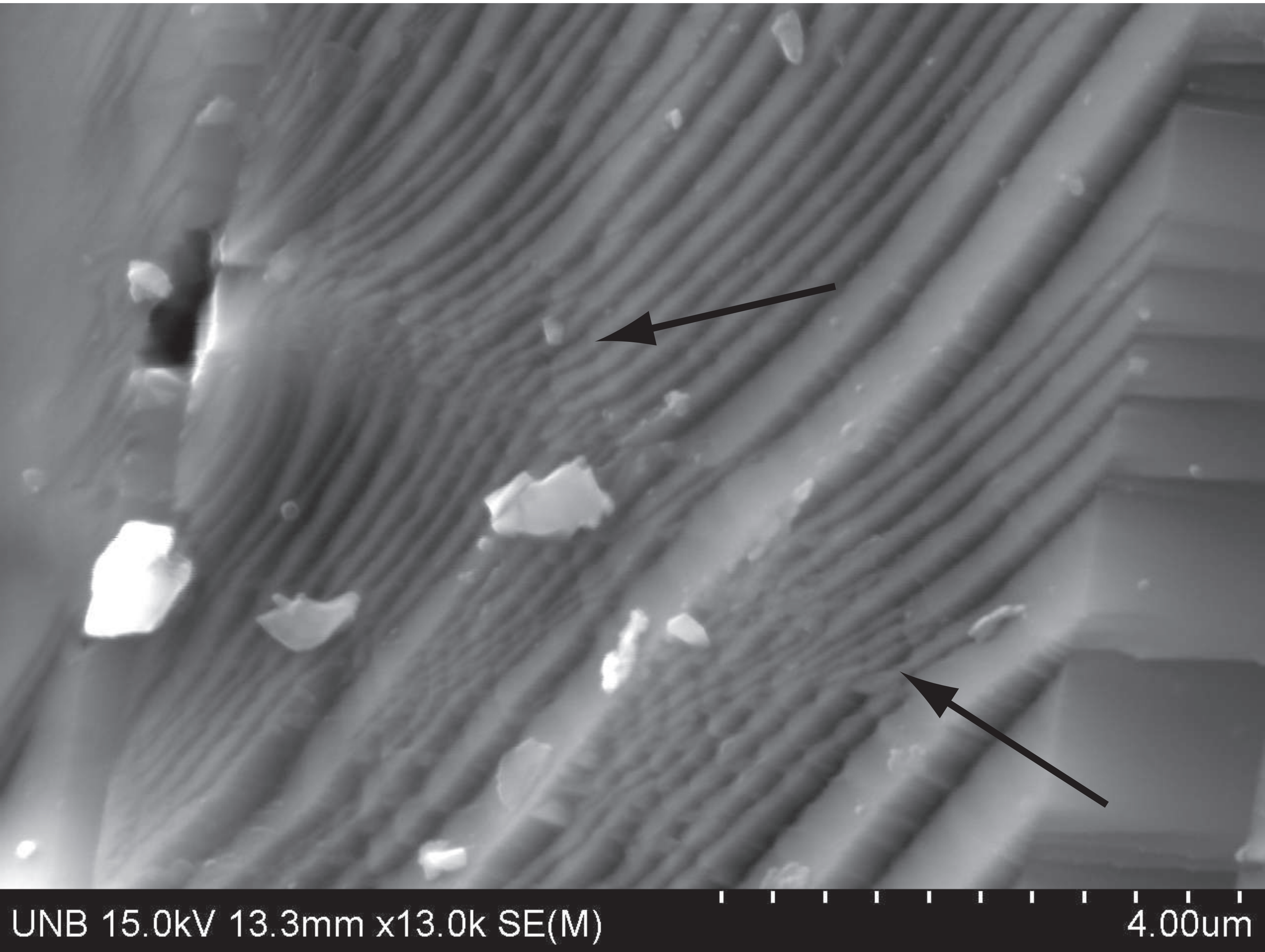

Fig. 10c. SEM image of dynamic fracture features in plagioclase.

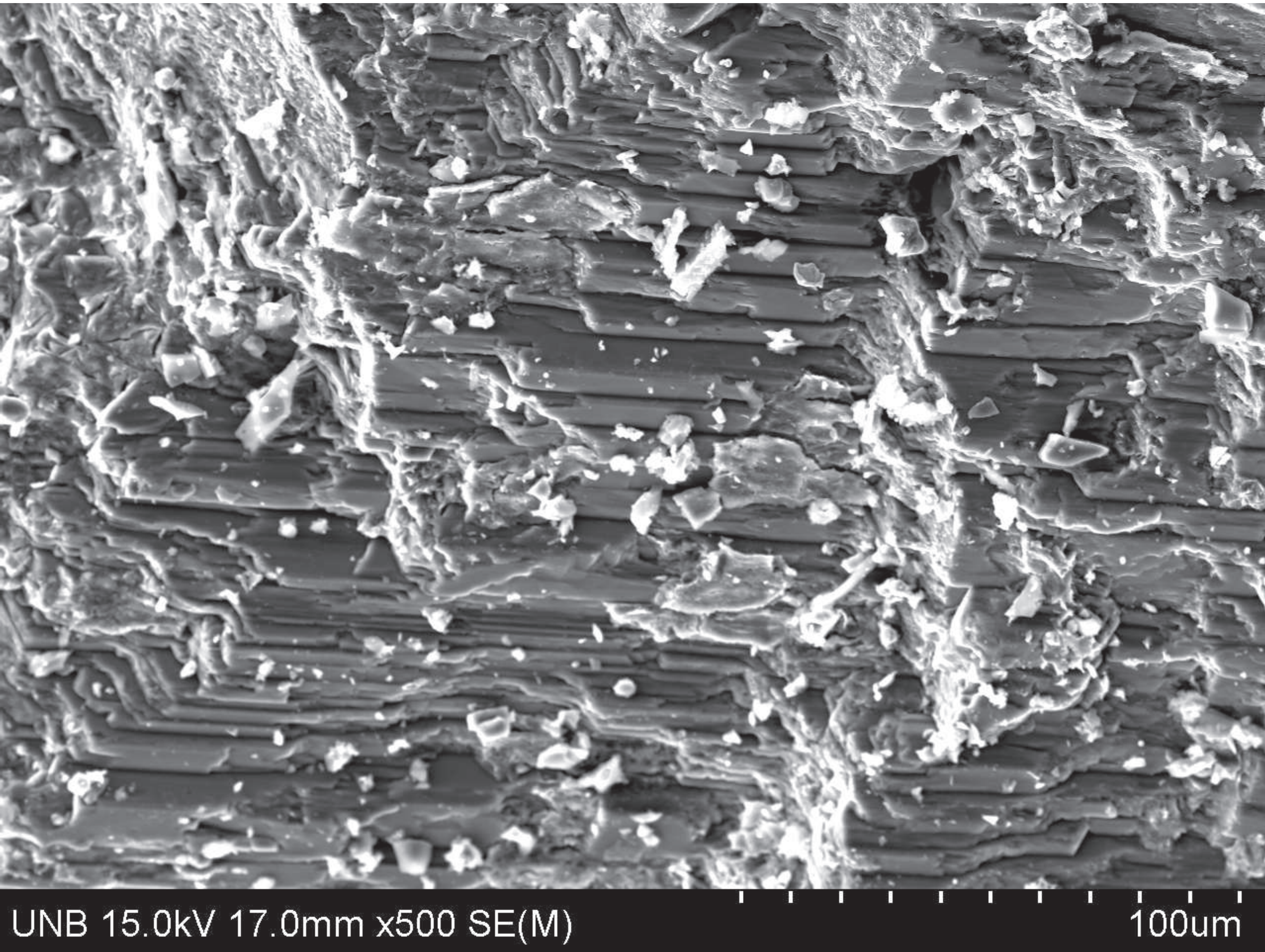

Fig. 10d. SEM image of melt-coated plagioclase surface.

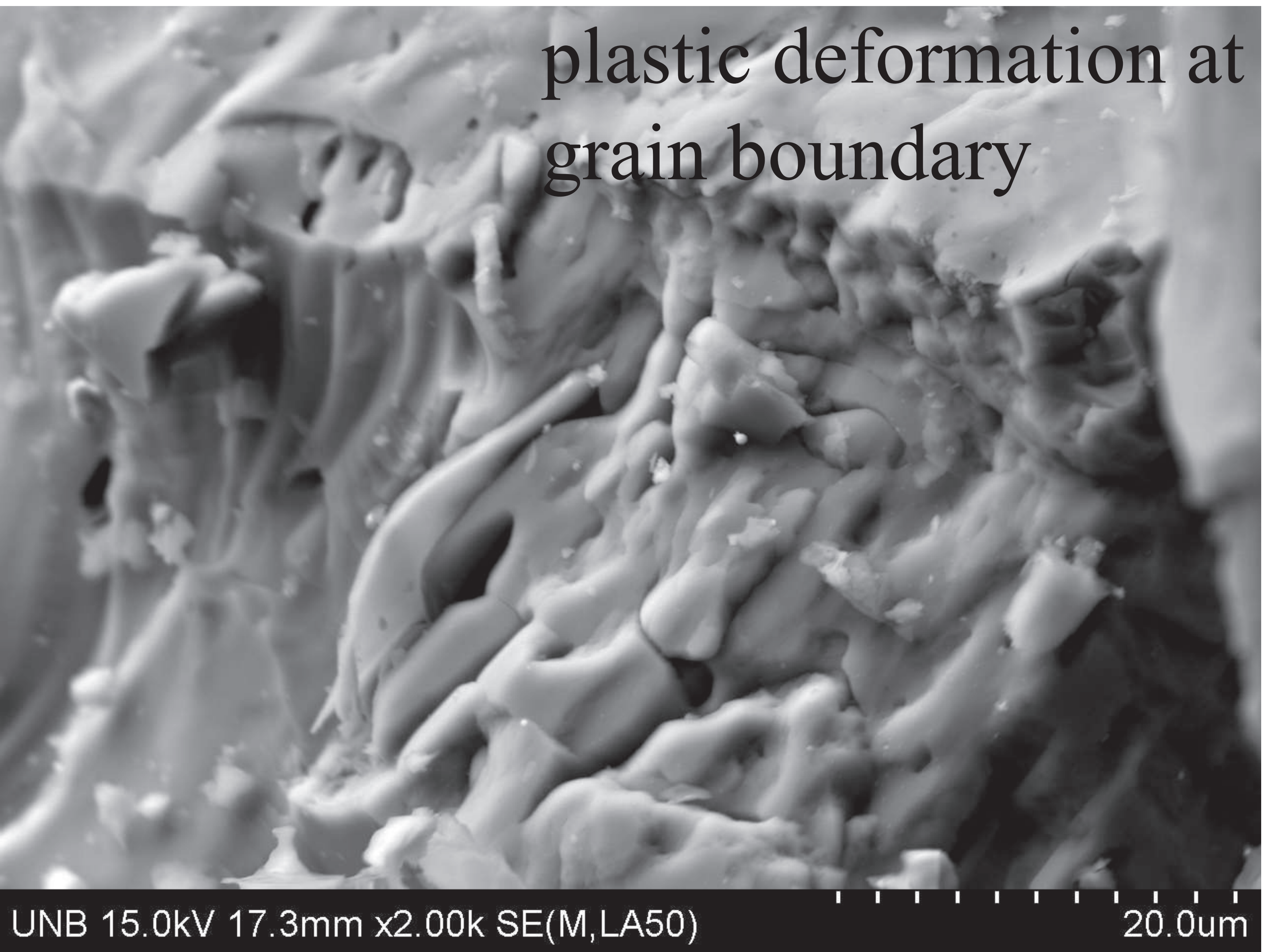

Fig. 10e. SEM image of dynamic fracture features in quartz.

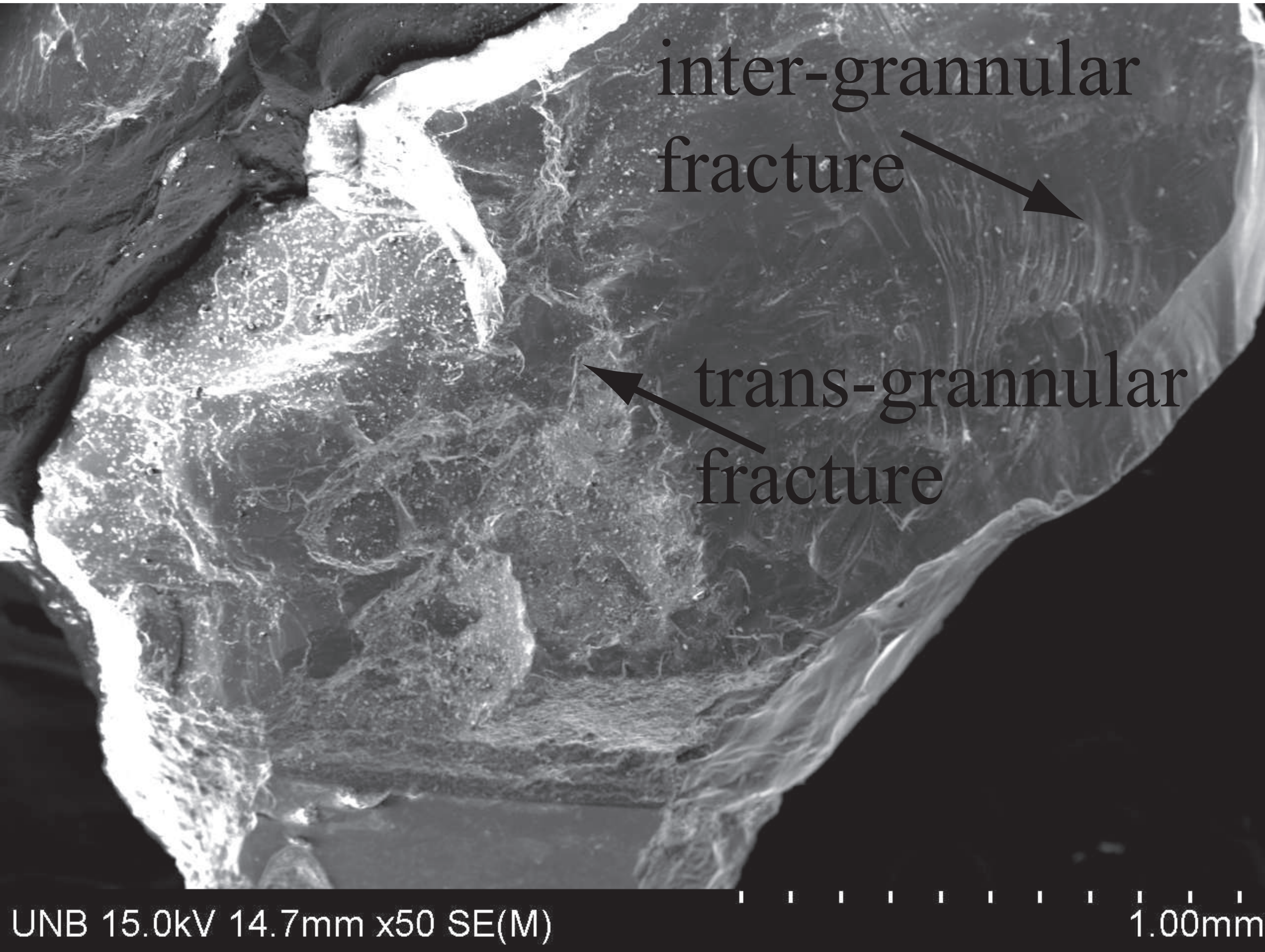

Fig. 10f. SEM image of micro-fault offset in quartz.

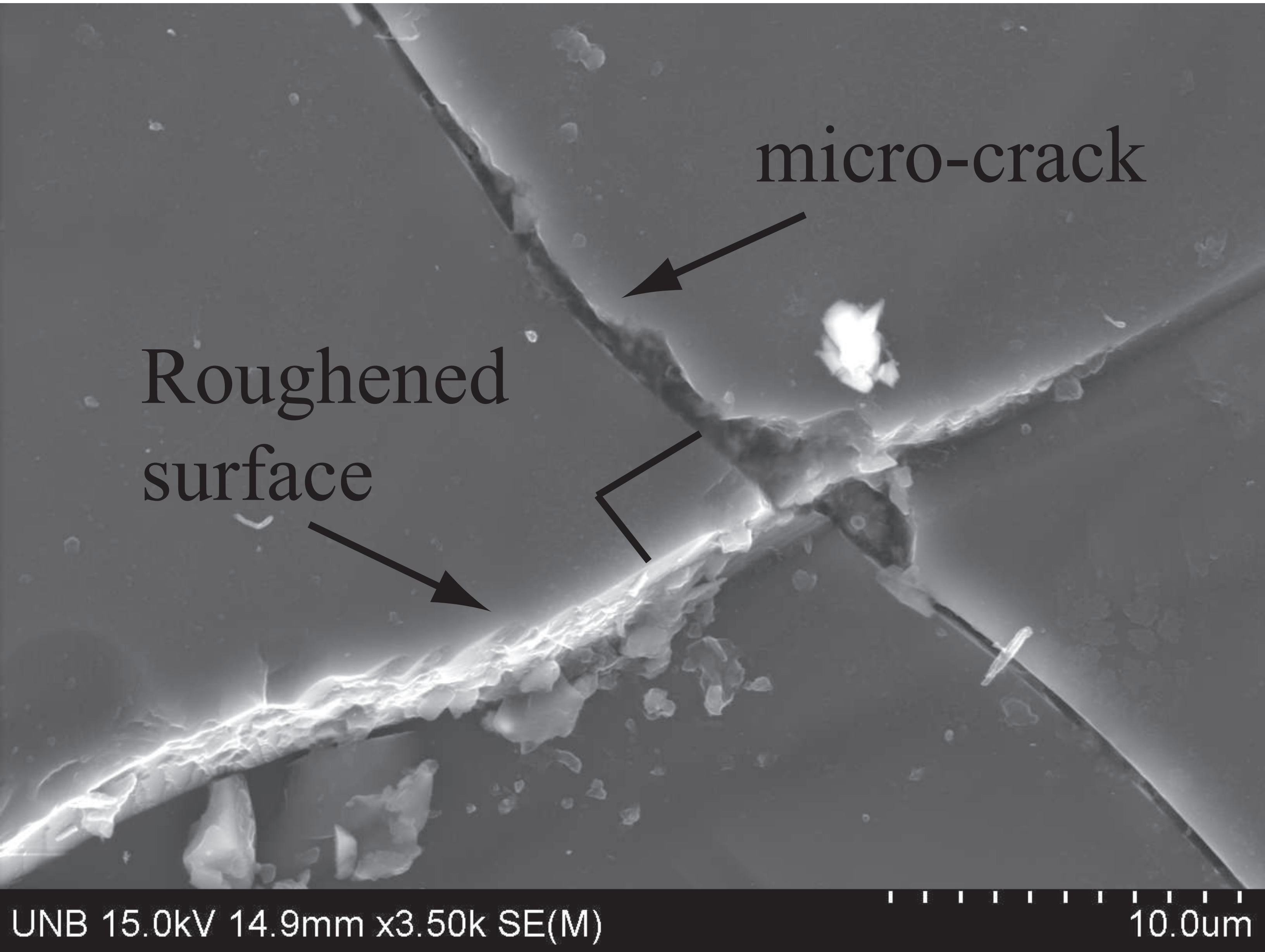

Fig. 11a. SEM image of localized melt in quartz micro-crack.

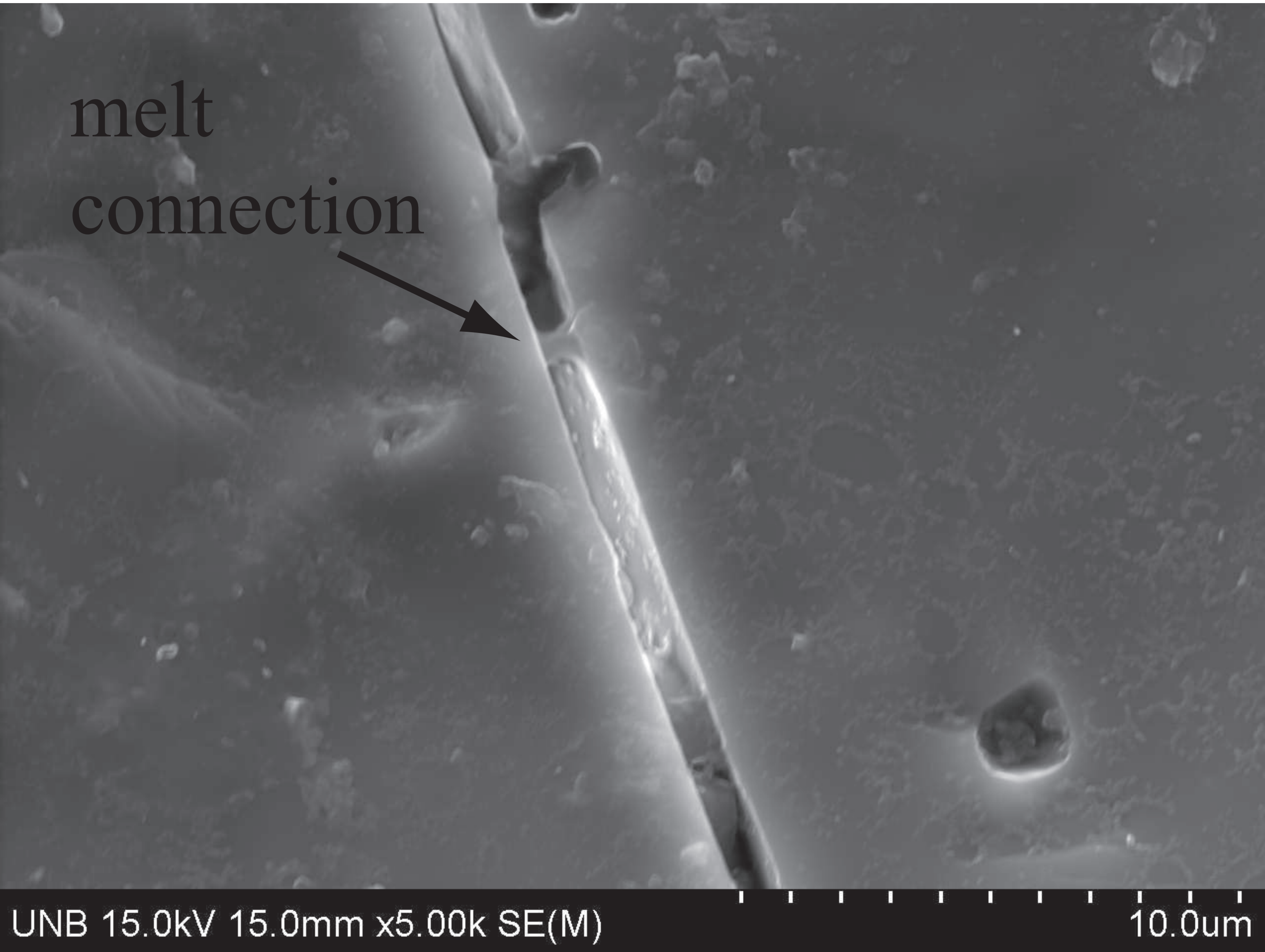

Fig. 11b. SEM image of titanium-oxide rich spheroid.

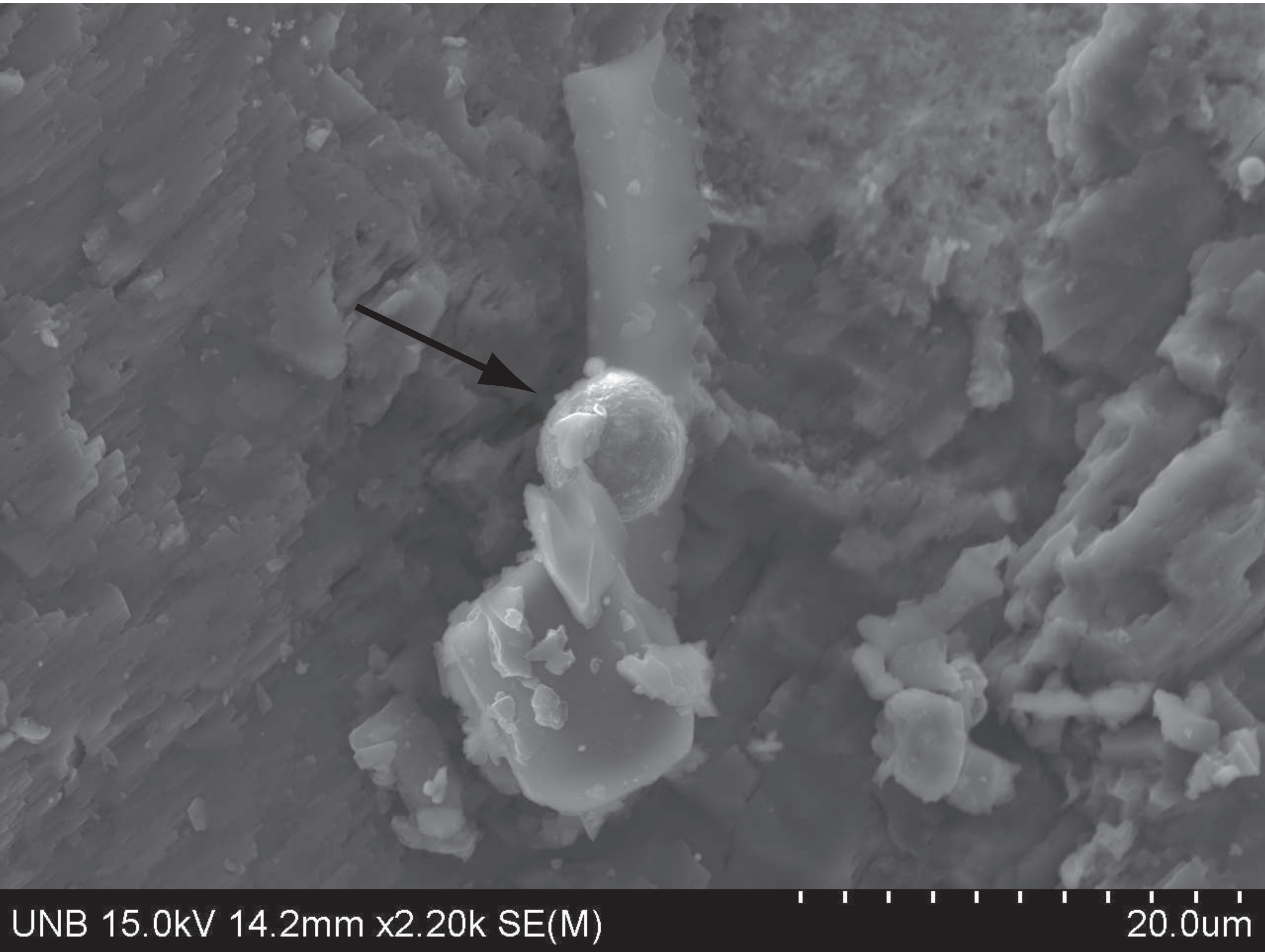

Fig. 11c. SEM image of plagioclase-like spheroid.

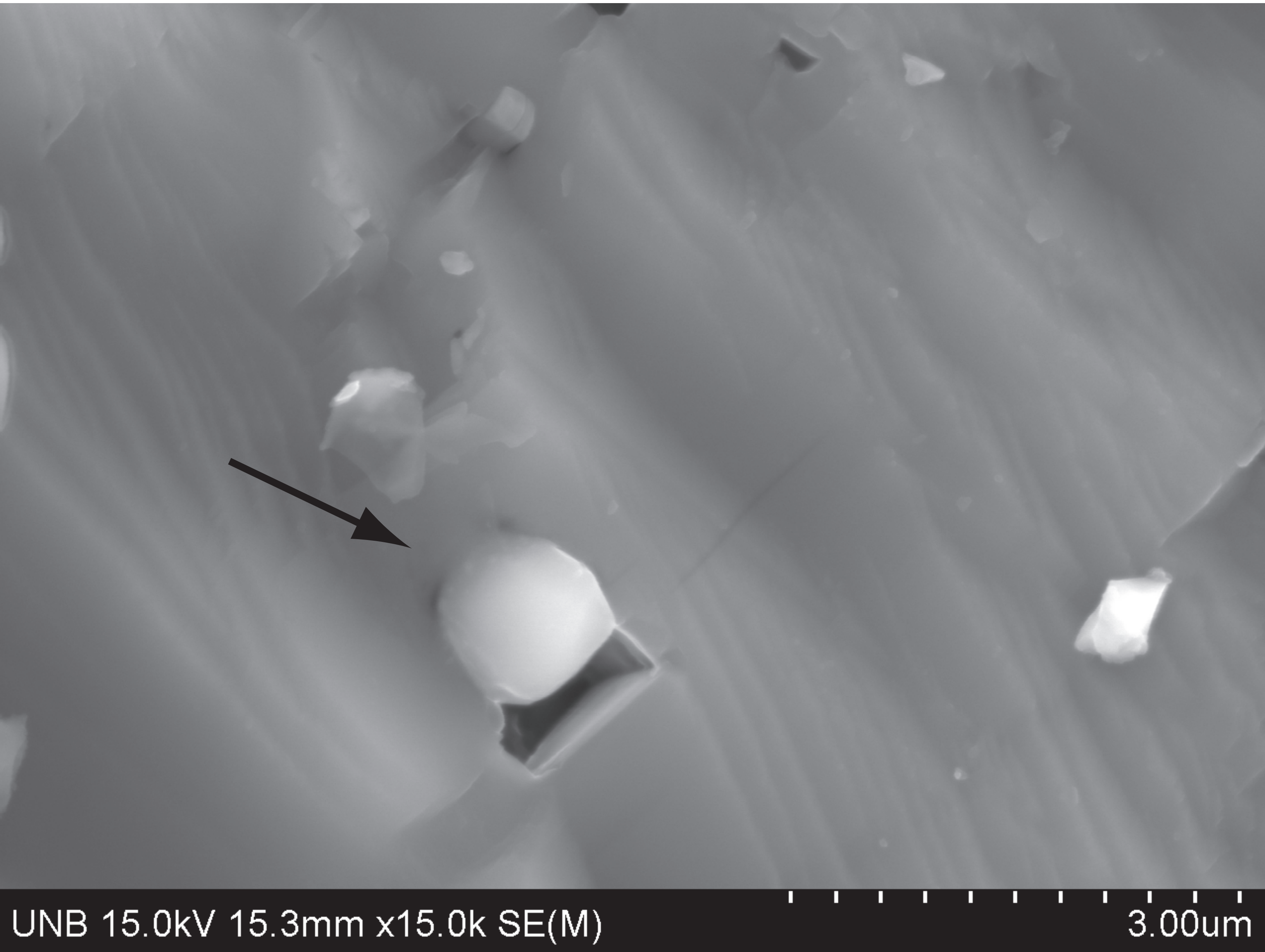

Fig. 11d. SEM image of alkali-feldspar-like spheroid.

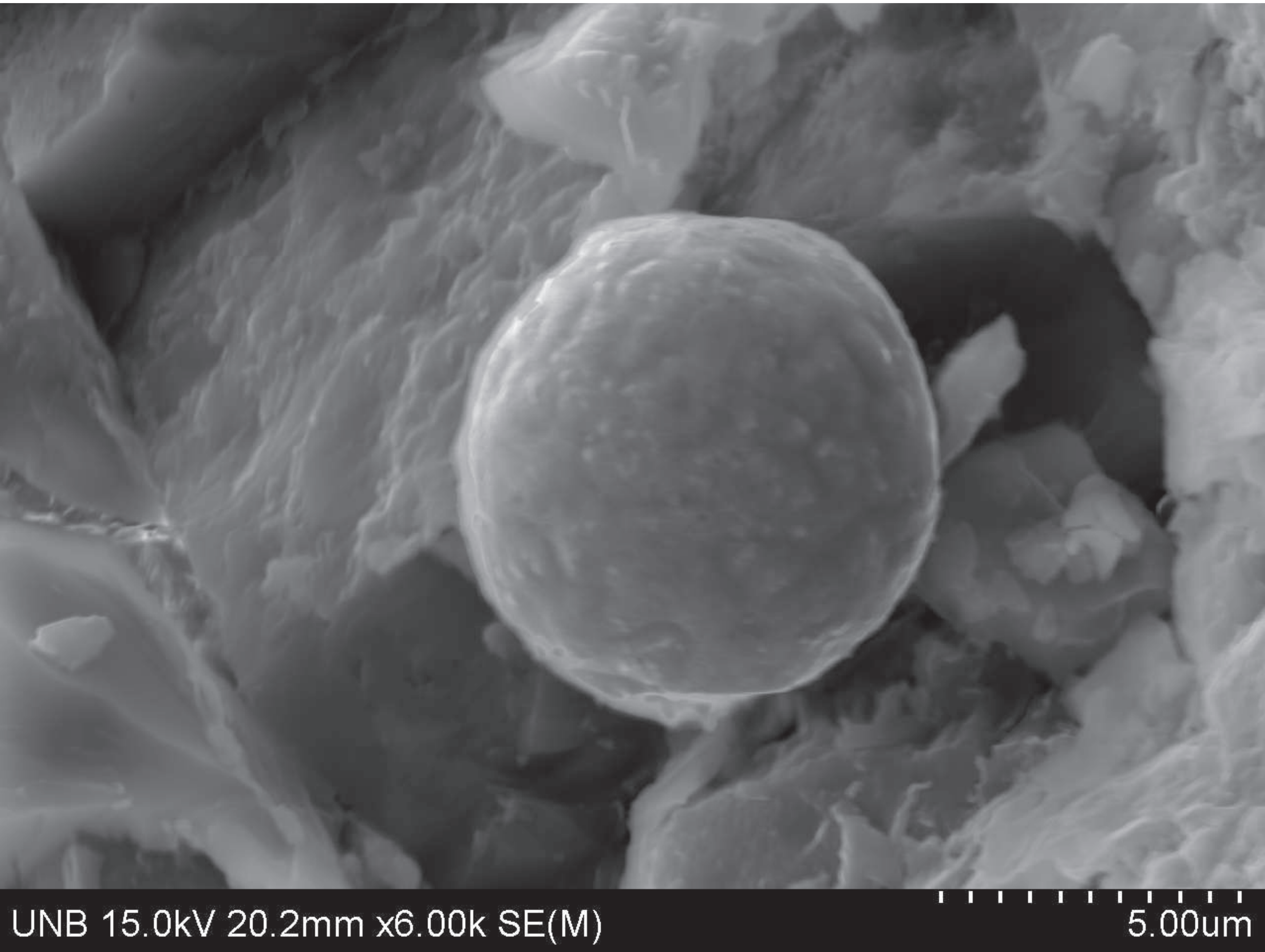

Fig. 11e. SEM image of alkali-feldspar-like spheroid.

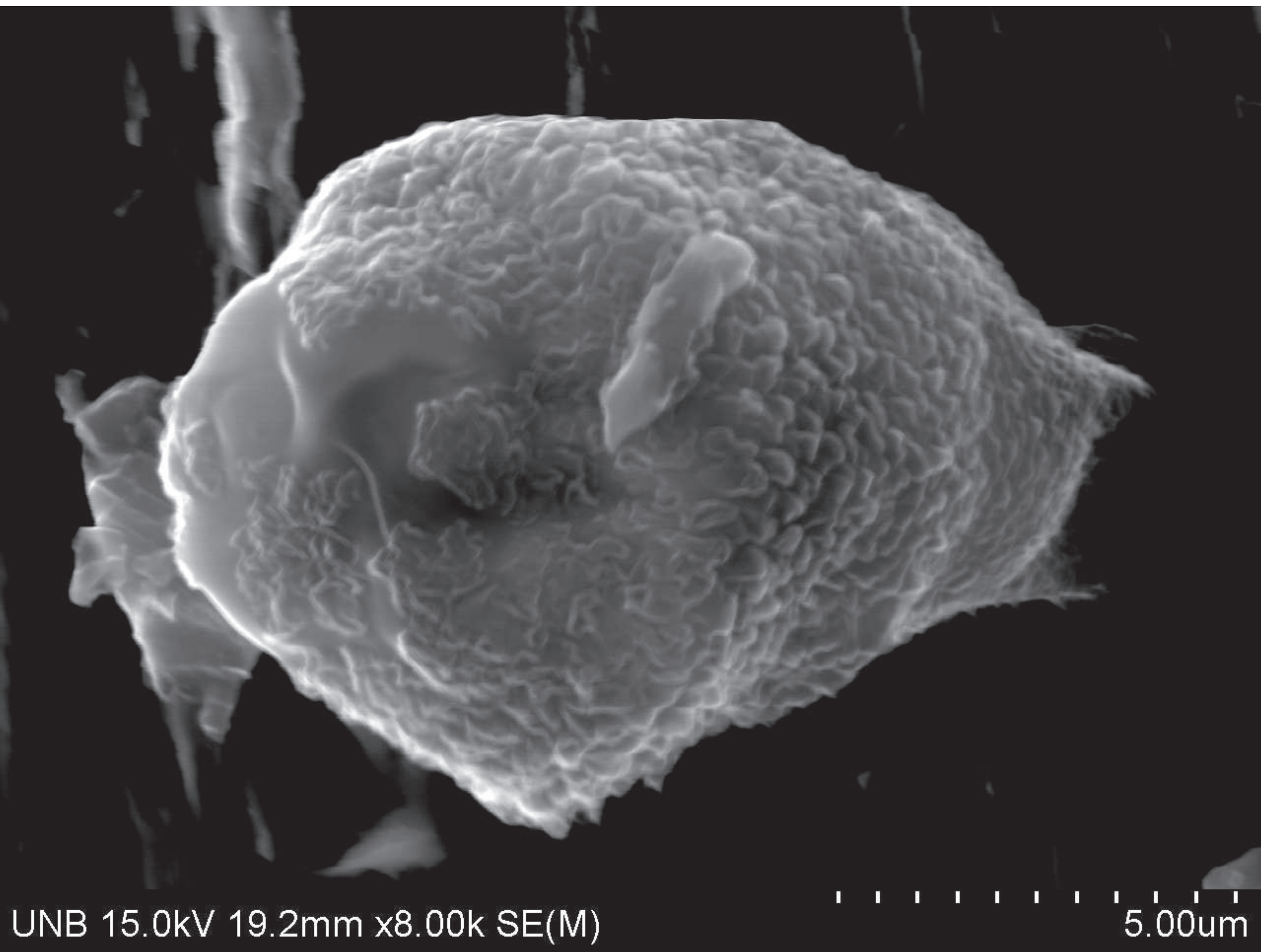

Fig. 11f. SEM image of CuO spheroid.